J. Fluid Mech. (2015), vol. 778, pp. 389–427.
doi:10.1017/jfm.2015.387

Modal and non-modal stability of boundary layers forced by spanwise wall oscillations

M. J. Philipp Hack[1],‡ **and Tamer A. Zaki**[1,2],†

[1]Department of Mechanical Engineering, Imperial College, London SW7 2AZ, UK
[2]Department of Mechanical Engineering, Johns Hopkins University, Baltimore, MD 21218, USA

(Received 13 October 2014; revised 6 May 2015; accepted 1 July 2015;
first published online 3 August 2015)

Modal and non-modal perturbation growth in boundary layers subjected to time-harmonic spanwise wall motion are examined. The superposition of the streamwise Blasius flow and the spanwise Stokes layer can lead to strong modal amplification during intervals of the base-flow period. Linear stability analysis of frozen phases of the base state demonstrates that this growth is due to an inviscid instability, which is related to the inflection points of the spanwise Stokes layer. The generation of new inflection points at the wall and their propagation towards the free stream leads to mode crossing when tracing the most unstable mode as a function of phase. The fundamental mode computed in Floquet analysis has a considerably lower growth rate than the instantaneous eigenfunctions. Furthermore, the algebraic lift-up mechanism that causes the formation of Klebanoff streaks is examined in transient growth analyses. The wall forcing significantly weakens the wall-normal velocity perturbations associated with lift-up. This effect is attributed to the formation of a pressure field which redistributes energy from the wall-normal to the spanwise velocity perturbations. The results from linear theory explain observations from direct numerical simulations of breakdown to turbulence in the same flow configuration by Hack & Zaki (*J. Fluid Mech.*, vol. 760, 2014*a*, pp. 63–94). When bypass mechanisms are dominant, the flow is stabilized due to the weaker non-modal growth. However, at high amplitudes of wall oscillation, transition is promoted due to fast growth of the modal instability.

Key words: boundary layer stability, transition to turbulence

1. Introduction

The influence of time-harmonic spanwise wall oscillation on bounded shear flows has been of interest due to its favourable impact on turbulent drag. Much of that literature has focused on turbulent channel flow, with fewer efforts dedicated to turbulent boundary layers. In the former case, higher amplitude of the wall motion at the optimal wall-oscillation frequency generally yields enhanced drag reduction. In transitional boundary layers, on the other hand, the influence of spanwise wall

---

† Email address for correspondence: t.zaki@jhu.edu

‡ Present address: Center for Turbulence Research, Stanford University, Stanford, CA 94305, USA.

oscillation is more variable. As shown by Hack & Zaki (2014*a*), it can stabilize the boundary layer or cause early transition to turbulence. Even at the optimal actuation frequency, increasing the amplitude of the wall motion can cause transition to swiftly move far upstream, ahead of the location of breakdown in the reference flow without wall oscillation. Since the base flow includes a spanwise unsteady component added to a streamwise boundary layer, instabilities of time-harmonic base states, cross-flow instability and bypass transition in two-dimensional boundary layers are all relevant, and are reviewed briefly.

1.1. *Instability of time-harmonic flows*

Earlier studies have established a profound effect of harmonic motions on the stability of various flows (Davis 1976). Experimental evidence of a destabilization in purely oscillatory pipe flow was provided by Clarion & Pelissier (1975), as well as Merkli & Thomann (1975) and Hino, Sawamoto & Takasu (1976). The latter work reported a sudden transition to turbulence during the deceleration phase of the flow, with subsequent relaminarization during the acceleration phase – results that were later confirmed by Akhavan, Kamm & Shapiro (1991). They found that in the first half of the acceleration interval, the production of turbulent kinetic energy was substantially reduced and the observed velocity profiles were in good agreement with laminar theory. During the deceleration phase, a rapid production of turbulent kinetic energy, which originated in the near-wall region, was observed.

For time-harmonic flows, stability is often defined in a global sense: a flow is considered unstable if the amplitude of a perturbation after a full period of the base state is larger than it was initially, and stable otherwise. Mathematically, the global stability of a time-harmonic flow is governed by the sign of the largest Floquet multiplier. Cowley (1987) nonetheless demonstrated that even though a base flow is Floquet stable, it can support substantial perturbation growth during parts of a period, followed by decay. Perturbations may therefore reach sufficiently high amplitudes to excite nonlinear mechanisms that induce breakdown to turbulence. Von Kerczek & Davis (1974) conducted linear stability analyses of a Stokes layer with zero mean component and found the flow to be stable for $Re_{Stokes} < 400$, where $Re_{Stokes} \equiv W_0\sqrt{T/\pi\nu}$ and W_0 and T are the amplitude and the period of the wall oscillation. Hall (1978) extended the investigation to semi-infinite domains but did not find evidence for an instability in the investigated range of Reynolds numbers, $Re_{Stokes} < 160$. Using the same computational approach, Blennerhassett & Bassom (2002) later demonstrated the existence of a critical Reynolds number, $Re_{Stokes} = 708$. Inviscid studies by Hall (2003) nonetheless indicated that the flow was stable in the limit $Re \rightarrow \infty$, implying a closed neutral curve that is delimited by a second critical Reynolds number beyond which perturbations become stable again. Thomas *et al.* (2011) studied the linear stability of streamwise oscillating channel flows. The addition of a steady mean profile was reported to change the stability characteristics and to increase the critical Reynolds number for global instability.

A common alternative approach to the analysis of time-periodic flows considers a series of frozen base states (Morkovin & Obremski 1969; Monkewitz & Bunster 1987). In this case, the coefficients of the linear perturbation equations are independent of time and therefore allow a normal-mode ansatz in that dimension. The instantaneous approach is justified in cases where the time scale of the instability is substantially shorter than that of the base state. A direct comparison between the growth rates computed from the instantaneous and Floquet approaches for a Stokes layer was

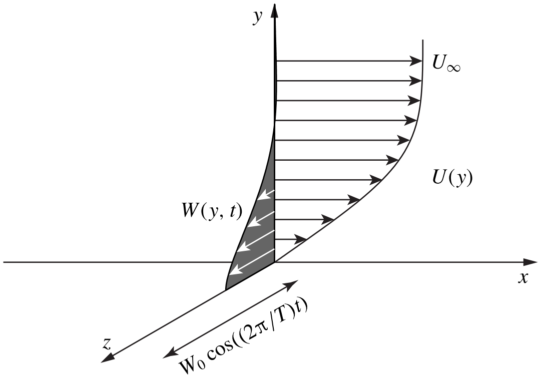

FIGURE 1. Schematic of the investigated base-flow configuration. The steady, streamwise boundary layer profile $U(y)$ is superimposed with an oscillatory component $W(y, t)$ due to the spanwise oscillatory wall forcing.

conducted by Luo & Wu (2010). It was shown that the instantaneous analysis presents an accurate approximation to the Floquet approach at moderate Reynolds numbers.

1.2. *Cross-flow instability*

In addition to being time-harmonic, the present base flow is also three-dimensional. The superposition of the unsteady spanwise Stokes-type layer with the streamwise Blasius profile leads to a complex flow configuration that gives rise to wall-normal inflection points (see figure 1). Three-dimensionality of the base state can lead to instability akin to cross-flow modes in the flow over swept wings. In that configuration, the local pressure gradient induces a flow component near the wall which is perpendicular to the free-stream velocity vector. The associated velocity profile is inflectional in the wall-normal direction and thus supports the amplification of an inviscid instability (see Bippes 1999; Saric, Reed & White 2003, for comprehensive reviews).

The cross-flow instability can be manifest as stationary or travelling waves. The former are characterized by wavefronts parallel to the local streamlines, while travelling waves are oblique, i.e. their wavefronts are aligned at an angle to the local velocity vector (Deyhle, Hoehler & Bippes 1993). The prevalence of either type is closely related to the receptivity to external perturbations. Experimental results by Deyhle & Bippes (1996) and Radeztsky, Reibert & Saric (1999) show that very low levels of free-stream turbulence intensity, $Tu_\infty < 0.15\,\%$, favour stationary waves, while travelling waves are observed for higher turbulence levels. Steady cross-flow modes can also be initiated by surface roughness (Schrader, Brandt & Henningson 2009).

During the initial linear stage of cross-flow instability, the wall-normal and transverse velocities of the mode displace the mean momentum of the boundary layer vertically, which leads to a perturbation that has most of its energy in the streamwise component. Once the streamwise component of the perturbation reaches a magnitude between 10 % and 30 % of the free-stream speed, the cross-flow perturbations begin to saturate due to nonlinear effects (Koch *et al.* 2000). Breakdown to turbulence is ultimately induced by high-frequency secondary instabilities (Wassermann & Kloker 2002; White & Saric 2005).

1.3. *Boundary layer streaks*

In the absence of a spanwise velocity component in the base state, a two-dimensional boundary layer is recovered. At moderate levels of free-stream perturbations, the natural transition mechanism via the exponential amplification of the Tollmien–Schlichting wave is bypassed by a more rapid process that involves the formation of highly energetic streaks inside the boundary layer. The streaks promote the amplification of high-frequency secondary instabilities which eventually initiate breakdown to turbulence. The generation of streaks via the lift-up mechanism relies on the presence of small wall-normal velocity perturbations, which vertically displace the mean flow and therefore create high-amplitude disturbances in the streamwise velocity component (Landahl 1975, 1980). When streaks are formed as the boundary layer response to forcing by free-stream turbulence, a path for the initial perturbation into the boundary layer is required. This prerequisite is non-trivial since vortical perturbations are generally unable to enter regions of mean shear (Hunt & Carruthers 1990). Previous studies have demonstrated that for Blasius boundary layers, streamwise elongated perturbations are least affected by the sheltering effect of the shear (Jacobs & Durbin 1998; Zaki & Saha 2009). For a general three-dimensional boundary layer profile, the wavenumber vector of the preferred disturbance is orthogonal to the mean shear (Hack & Zaki 2012).

The lift-up mechanism is independent of the modal stability of the flow, and is overcome by viscous decay at finite time (see e.g. Brandt 2014). This transient nature of non-modal growth means that there exists an upper bound for the resulting amplification of perturbation energy. In Blasius boundary layers, the optimal initial condition which yields the most energetic streaks is a pair of steady, streamwise oriented vortices (Butler & Farrell 1992; Andersson, Berggren & Henningson 1999). For the case of steady three-dimensional Falkner–Skan–Cooke boundary layers, Corbett & Bottaro (2001) found that streamwise elongated streaks remain the most energetic perturbations at subcritical conditions. Ricco (2011) examined the influence of a steady spanwise wall forcing on the lift-up mechanism. That work predicted that the amplification of steady streaks is reduced by the spanwise forcing. This effect is enhanced with growing W_0, until the streaks completely vanish. Duque-Daza *et al.* (2012) conducted linear analyses of perturbation growth in fully turbulent flow subject to forcing by streamwise travelling waves of spanwise wall velocity. Their results pointed to a correlation between the reduction of viscous drag and a weakening of turbulent streaks. A similar approach was adopted by Blesbois *et al.* (2013), who considered generalized optimal disturbances in turbulent channel flow with a spanwise oscillating wall. They found that the optimal perturbation is aligned at an angle relative to the instantaneous velocity vector.

The present study examines the linear instability mechanisms that are active in pre-transitional boundary layers forced by spanwise wall oscillations. The paper is structured as follows: § 2 concisely summarizes DNS results of the influence of spanwise wall forcing with different amplitudes on transitional boundary layers. Section 3 reports modal stability analyses of a zero-pressure-gradient boundary layer when a spanwise Stokes layer is superimposed on the flow. Section 4 focuses on the impact of the wall forcing on the non-modal lift-up effect that generates boundary layer streaks. The relationship between modal and non-modal growth is examined in § 5. Section 6 summarizes the final conclusions.

2. Observations from DNS of bypass transition with wall oscillation

The linear studies presented in this work are motivated by results from DNS of transitional boundary layers subjected to wall oscillation (Hack & Zaki 2014*a*). Since the nonlinear simulations are not the focus of the current work, they are discussed briefly and the relevant parameters are reported. Where beneficial, results from the DNS will be included in order to complement the linear analyses, and to ensure that the current presentation is complete and self-contained.

Previous simulations of bypass transition in two-dimensional boundary layers have adopted two approaches based on the location of the inflow plane relative to the leading edge. With the inflow plane downstream of the leading edge, Jacobs & Durbin (2001) formulated an inflow-synthesis method to prescribe free-stream turbulence. In contrast, Nagarajan, Lele & Ferziger (2007) included the leading edge in their computational domain. Their results showed that, for a slender leading edge, the methodology by Jacobs & Durbin (2001) accurately captures the downstream development of the boundary layer and bypass transition. The methodology was used by various authors (e.g. Brandt, Schlatter & Henningson 2004; Schrader *et al.* 2009; Schrader, Subir & Brandt 2010), and the results compared favourably to experiments both qualitatively and quantitatively (e.g. Matsubara & Alfredsson 2001; Mandal, Venkatakrishnan & Dey 2010). Downstream of the inlet, elongated boundary layer streaks amplify, with the low-speed streaks lifting towards the edge of the boundary layer. They undergo a secondary instability (Andersson *et al.* 2001; Vaughan & Zaki 2011; Hack & Zaki 2014*b*), followed by the formation of turbulence spots and full nonlinear breakdown to turbulence. The same approach for simulating bypass transition was adopted in the computations discussed herein, without and with spanwise wall oscillation imposed downstream of the inflow plane.

In all simulations, the inflow to the computational domain is located at distance $\tilde{x} = \tilde{x}_0$ from the leading edge. Lengths are normalized by the inlet 99 % boundary layer thickness, δ_0, and velocities are normalized by the free-stream value, U_∞. The inlet Reynolds number based on δ_0 is $Re_{\delta_0} = 800$ (in terms of the Blasius length scale, $\mathscr{L} = \sqrt{\tilde{x}\nu/U_\infty}$, the inlet Reynolds number is $Re_{\mathscr{L}_0} = 162$). For convenience, a streamwise coordinate $x \equiv \tilde{x} - \tilde{x}_0$ can be defined relative to the inlet plane. The turbulence intensity in the free stream is $Tu_\infty = 3\,\%$, and the spanwise forcing at the wall is applied by imposing the boundary condition $w(y=0, t) = W_0 \cos((2\pi/T)t)$ over the full extent of the simulation domain.

Parameter studies using DNS demonstrated that suitable choice of the amplitude and period of the wall forcing can substantially delay breakdown to turbulence (Hack & Zaki 2014*b*). The stabilization of the pre-transitional flow regime was associated with a significant weakening of the amplitude of boundary layer streaks. On the other hand, an increase of either W_0 or T beyond their respective optima resulted in an acceleration of the transition process, with breakdown to turbulence occurring in some of the cases significantly earlier than in an unforced reference simulation. This behaviour is captured in the top views of the DNS flow field presented in figure 2.

The contours in figure 2 mark the stochastic fluctuations, u', which are obtained from a triple decomposition of the flow field,

$$u_{DNS} = \rlap{\overbrace{\phantom{\bar{u} + \tilde{u}_{\varphi}}}^{\langle u \rangle_{\varphi}}}\bar{u} + \underbrace{\tilde{u}_{\varphi} + u'}_{u''} \tag{2.1}$$

with $\varphi = 1/T \bmod (t, T)$. Here, $\bar{u}$ denotes the spanwise and time-average, and $\tilde{u}_\varphi$ is the periodic component introduced by the time-harmonic wall-motion.

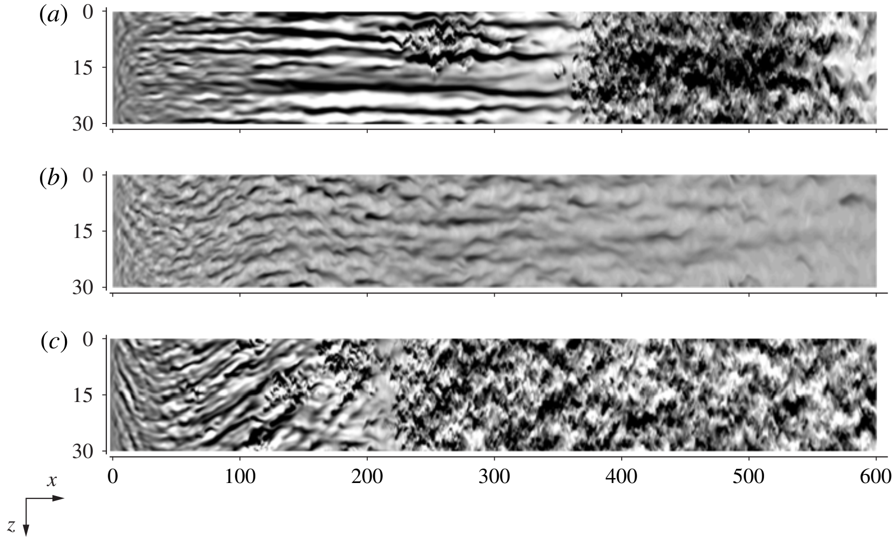

FIGURE 2. Top views of transitional boundary layers from DNS at $y/\delta(x) = 0.45$. Grey contours give the streamwise stochastic fluctuation from $u' = -0.12$ (black) to $u' = 0.12$ (white). (*a*) Reference case, $W_0 = 0.00$. (*b*) Wall forcing with amplitude $W_0 = 0.25$ and period $T = 200$. (*c*) Wall forcing with amplitude $W_0 = 0.40$ and period $T = 200$.

In the unforced reference simulation (figure 2*a*), the boundary layer develops clearly discernible streaks, represented by streamwise elongated regions of positive and negative u'. An isolated turbulent spot is observed at $x \approx 250$, and the flow becomes fully turbulent at $x \approx 380$. The forced case with parameters $T = 200$, $W_0 = 0.25$ (figure 2*b*) shows a different behaviour that is characterized by the absence of pronounced streak growth. The flow is laminar over the full length of the domain, $2.6 \times 10^4 \leqslant Re_{\tilde{x}} \leqslant 5.0 \times 10^4$. This stabilization is reversed at the higher forcing amplitude $W_0 = 0.40$, as demonstrated in the last frame (figure 2*c*), where turbulent spots are observed as early as $x \approx 120$. While a significant perturbation level is reached upstream of transition, the associated disturbances are of relatively high frequency and thus clearly differ from elongated boundary layer streaks, which are associated with classical bypass breakdown. Hence the parameters of the spanwise wall forcing not only govern the downstream location of transition to turbulence, but also the underlying mechanism. In the remainder of this work, linear analysis is applied in order to explain this behaviour.

3. Modal instability

Modal linear stability analysis is performed in this section, and is aimed at evaluating the potential role of exponential instabilities when spanwise wall motion is superimposed onto the streamwise boundary layer flow. Particular interest is in the case of relatively high $Re_{Stokes} \equiv W_0\sqrt{T/\pi\nu}$, where breakdown to turbulence is accelerated (figure 2*c*). Evidence of modal instability in the DNS is presented first, and is followed by linear analysis of instantaneous base-state profiles in order to explain the origin of this instability.

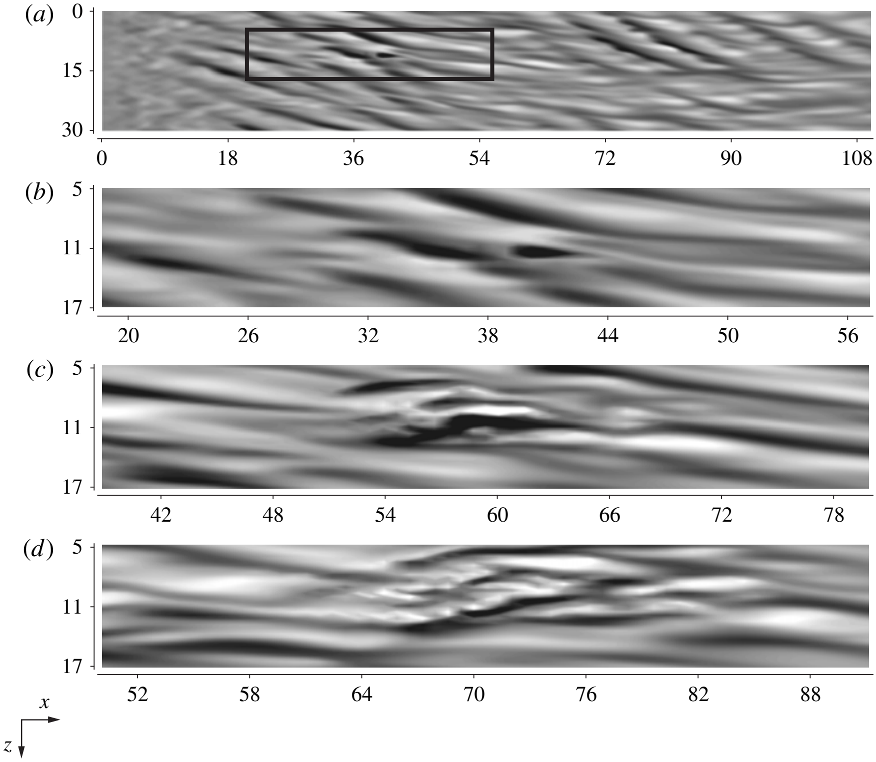

FIGURE 3. Time series of a spot precursor for forcing parameters $T = 200$, $W = 0.40$ at $y/\delta(x) = 0.40$: (*a*) $t = 0$; (*b*) $t = 0$; (*c*) $t = 38$; (*d*) $t = 58$. Contours give the streamwise velocity fluctuation, from $u' = -0.20$ (black) to $u' = 0.20$ (white).

3.1. *Evidence of modal instability in DNS*

When the amplitude of the wall motion is high, $W_0 = 0.40$, direct simulations predict an early breakdown to turbulence (figure 2*c*). In order to determine the origin of these breakdown events, figure 3 provides a time series of the precursors to the onset of a turbulent spot from that simulation. The topmost frame shows the full width of the computational domain upstream of transition to turbulence and demonstrates the presence of a perturbation field of relatively high amplitude inside the boundary layer. The streamwise extent of the perturbations is similar to the local boundary layer thickness and is thus at least an order of magnitude smaller than that of typical boundary layer streaks. The detailed views shown in the remaining frames indicate that the perturbation takes the form of a localized wavepacket, which ultimately breaks down into a turbulent spot.

The observed breakdown scenario differs qualitatively from the classical bypass mechanism. In order to quantitatively elucidate the role of short-scale structures, the spectral content of the fluctuation field is examined in a time series of 4000 snapshots of the flow field in planes parallel to the wall. A Hann window is used for the streamwise dimension. The time difference between two consecutive samples is two time units, and the complete time series therefore spans $N = 20$ wall-oscillation periods. The analysis considers the wall-normal fluctuation field, v', in the pre-transitional region ($75 < x < 130$ and $0.84 \times 10^5 \leqslant Re_{\tilde{x}} \leqslant 1.30 \times 10^5$). The

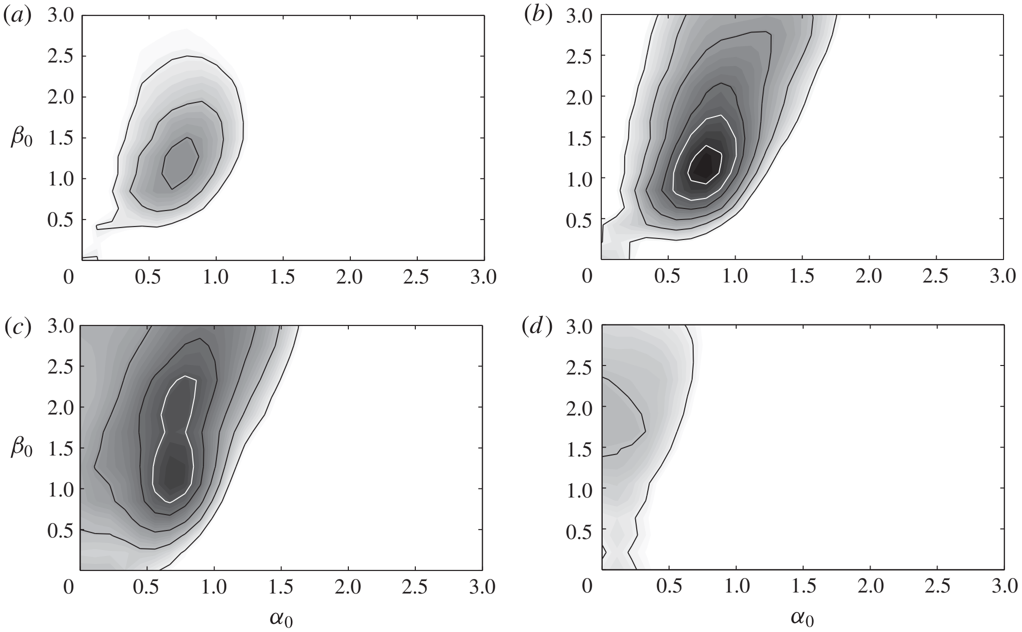

FIGURE 4. Contours of $\|\hat{v}_\varphi\|$ as a function of the streamwise and spanwise wavenumbers, parametrized by the phase of the base state: (*a*) $\varphi = 0$; (*b*) $\varphi = 0.125$; (*c*) $\varphi = 0.250$; (*d*) $\varphi = 0.375$.

dependence on the phase of the base flow is preserved by evaluating the spectral decomposition as a function of the parameter φ,

$$\hat{v}_\varphi(\alpha, \beta) = \frac{1}{N}\sum_{n=1}^{N}\int_{-\infty}^{\infty}\int_{-\infty}^{\infty} v'(\varphi)\exp(-2\pi\mathrm{i}(\alpha x + \beta z))\,\mathrm{d}x\,\mathrm{d}z. \tag{3.1}$$

The magnitudes of the Fourier coefficients, $\|\hat{v}_\varphi\|$, are presented in figure 4 for $\varphi = \{0, 0.125, 0.250, 0.375\}$ as a function of the streamwise and spanwise wavenumber normalized by the inlet boundary layer thickness, $\alpha_0 = \alpha\delta_0$ and $\beta_0 = \beta\delta_0$. The results demonstrate that the phase of the base flow has an appreciable effect on the perturbation magnitude as well as on the location of the peak in the wavenumber plane. The most energetic perturbations are observed at $\varphi = 0.125$ and $(\alpha_0, \beta_0) \approx (0.8, 1.2)$.

In order to substantiate the influence of the phase of the base flow on the perturbation field, figure 5 provides phase-averaged space–time diagrams. The contours are the standard deviation, $\langle u'\rangle_{rms}$, of the fluctuation field in a plane located at 30 % of the local boundary layer thickness,

$$\langle u'\rangle_{rms} = \left(\frac{1}{NL_z}\sum_{N}\int_0^{L_z} u'^2\,\mathrm{d}z\right)^{1/2} \tag{3.2}$$

where L_z is the spanwise extent of the computational domain and $N = 20$ is the number of sampled periods of the base flow. Results for the streamwise velocity component

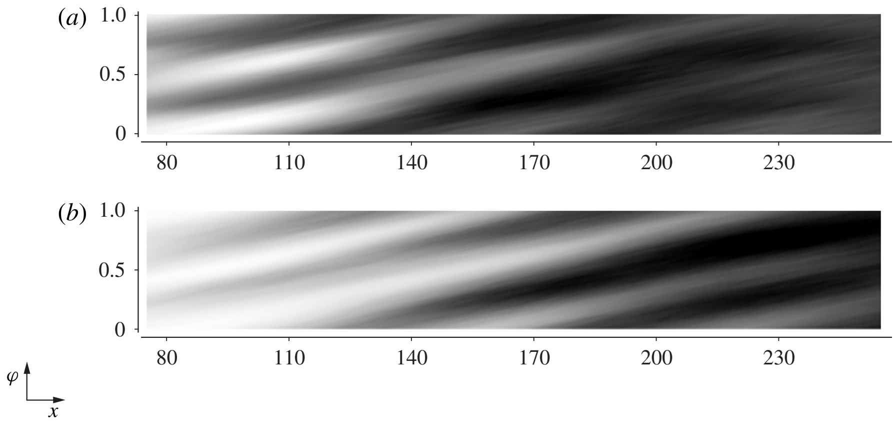

FIGURE 5. Phase-averaged space–time diagrams at $y/\delta(x) = 0.30$. Wall oscillation with $T = 200$, $W_0 = 0.40$. (*a*) Streamwise component, $\langle u' \rangle_{rms}$. (*b*) Wall-normal component, $\langle v' \rangle_{rms}$. Reproduced from Hack & Zaki (2014*a*).

are shown in figure 5(*a*). Alternating bands of high and low $\langle u' \rangle_{rms}$ are observed with half the period of the wall oscillation. In other words, each forcing period contains two intervals during which the fluctuations amplify, separated by intervals during which the fluctuations decay again. The bands are aligned at an angle to the abscissa, which corresponds to a characteristic 'speed' $c_c \approx 0.60$ with which the perturbation field travels downstream. As the flow becomes increasingly turbulent, the bands smear out and finally form a continuous region of high $\langle u' \rangle_{rms}$.

The standard deviation of the wall-normal velocity fluctuation v' shows a very similar behaviour (see figure 5*b*). While the magnitude of $\langle v' \rangle_{rms}$ is initially lower than $\langle u' \rangle_{rms}$, the observed angle of the bands is nearly identical. The agreement between the phases of the streamwise and wall-normal fluctuations indicates a simultaneous amplification and decay of the two components.

The phase dependence of the transition process is also reflected in the phase-averaged skin friction coefficient,

$$\langle C_f \rangle_\varphi = \frac{\mu \left. \dfrac{\partial \langle u \rangle_\varphi}{\partial y} \right|_{y=0}}{\frac{1}{2} \rho U_\infty^2}, \tag{3.3}$$

which is reported in figure 6 as a function of the downstream coordinate. For each phase, the $\langle C_f \rangle_\varphi$ curve exhibits an oscillation in the transition region, which is in contrast to the monotonic rise in the reference case without wall forcing. These local extrema are evidence that breakdown, and potentially the flow instability, are phase dependent. By relating the downstream positions of the peaks observed at different phases, the characteristic speed $c_c = 0.60$, which was observed in figure 5, is recovered.

The observations from DNS summarized in this section relate the early breakdown observed at $W_0 = 0.40$ and $T = 200$ to a mechanism that qualitatively differs from conventional bypass transition which takes place via the amplification and secondary instability of low-frequency streaks. Instead, the length scale of the relevant instability is of the order of the boundary layer thickness, and its growth depends on the phase

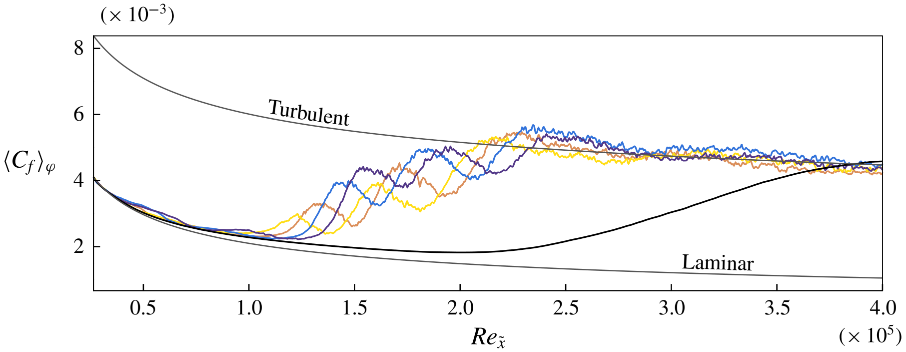

FIGURE 6. (Colour online) Phase-averaged skin friction coefficient for wall oscillation with $T = 200$, $W_0 = 0.40$, evaluated at $\varphi = 0.00$ (yellow, lightest), $\varphi = 0.125$ (red), $\varphi = 0.250$ (blue), $\varphi = 0.375$ (purple, darkest). The black line represents an unforced reference case.

of the base flow. In the following, the nature of this instability is explored using linear stability theory.

3.2. *Instantaneous stability analysis*

In order to examine the role of modal growth mechanisms, the linear stability of a base flow which is a superposition of a streamwise zero-pressure-gradient boundary layer and a transverse Stokes layer is investigated. The presence of the streamwise boundary layer causes a minor deviation of the spanwise velocity profile from the analytical solution of the Stokes second problem, given by

$$W_{analytical}(y, t) = W_0 \exp\left(-\sqrt{\frac{\pi}{\nu T}}y\right) \cos\left(\frac{2\pi}{T}t - \sqrt{\frac{\pi}{\nu T}}y\right). \tag{3.4}$$

Although the resulting difference in the stability characteristics is relatively small, the following analyses adopt a base state which is obtained from laminar-flow simulations of a boundary layer atop an oscillating flat plate without free-stream turbulence. This base flow will be referred to as a 'Blasius–Stokes' profile. The spanwise component, $\tilde{w}$, is the phase average in the triple decomposition (2.1). An instantaneous approach is pursued, and the instability analysis is applied to frozen phases of the time-harmonic flow. The base state of the analysis depends on the wall-normal coordinate only, $\boldsymbol{U} = (U(y),\ 0,\ W(y))^{\mathrm{T}}$. The instability is represented by its wall-normal velocity, v', and wall-normal vorticity, η'. The time evolution of the associated state vector, $\boldsymbol{q}' \equiv (v', \eta')^{\mathrm{T}}$, is governed by

$$\left(\frac{\partial}{\partial t} + U\frac{\partial}{\partial x} + W\frac{\partial}{\partial z}\right)\nabla^2 v' - \frac{\partial^2 U}{\partial y^2}\frac{\partial v'}{\partial x} - \frac{\partial^2 W}{\partial y^2}\frac{\partial v'}{\partial z} = -\frac{\partial}{\partial y}\nabla^2 p' + \frac{1}{Re}\nabla^4 v', \tag{3.5}$$

$$\left[\frac{\partial}{\partial t} + U\frac{\partial}{\partial x} + W\frac{\partial}{\partial z} - \frac{1}{Re}\nabla^2\right]\eta' = \frac{\partial v'}{\partial x}\frac{\partial W}{\partial y} - \frac{\partial v'}{\partial z}\frac{\partial U}{\partial y}. \tag{3.6}$$

The perturbation field is assumed to be periodic in the streamwise and spanwise dimensions with wavenumbers α and β, respectively. Unless otherwise stated, the reference length scale is the local 99 % thickness of the boundary layer, δ, and velocities are normalized by the free-stream value, U_∞. A normal-mode assumption is introduced in time, $\boldsymbol{q}'(t)=\boldsymbol{q}\exp(\mathrm{i}\sigma t)$. The full ansatz for the instability is, therefore,

$$v'(x, y, z, t) = v(y)\exp(\mathrm{i}(\alpha x+\beta z-\sigma t)) \tag{3.7}$$

$$\eta'(x, y, z, t) = \eta(y)\exp(\mathrm{i}(\alpha x+\beta z-\sigma t)), \tag{3.8}$$

and (3.5) and (3.6) become

$$\left[(-\mathrm{i}\sigma+\mathrm{i}\alpha U+\mathrm{i}\beta W)(\mathscr{D}^2-k^2)-\mathrm{i}\alpha\mathscr{D}^2U-\mathrm{i}\beta\mathscr{D}^2W-\frac{1}{Re}(\mathscr{D}^2-k^2)^2\right]v=0, \tag{3.9}$$

$$\left[-\mathrm{i}\sigma+\mathrm{i}\alpha U+\mathrm{i}\beta W-\frac{1}{Re}(\mathscr{D}^2-k^2)\right]\eta=\mathrm{i}(\alpha\mathscr{D}W-\beta\mathscr{D}U)v \tag{3.10}$$

with $\mathscr{D}\equiv\partial/\partial y$ and $k^2\equiv\alpha^2+\beta^2$. A temporal stability analysis is performed where the unknown quantity is the complex frequency σ, while the modal wavenumbers α and β are known, real-valued parameters. The implicit assumption is that the growth rate of the instability is faster than the change in the base flow. The numerical solution of (3.9) and (3.10) uses a Chebyshev expansion in the wall-normal dimension. The generalized eigenvalue problem of the form $\boldsymbol{A}\boldsymbol{q}=\sigma\boldsymbol{B}\boldsymbol{q}$ is solved through a Schur decomposition, such that $\boldsymbol{A}=\boldsymbol{Q}\boldsymbol{S}\boldsymbol{Z}^H$ and $\boldsymbol{B}=\boldsymbol{Q}\boldsymbol{T}\boldsymbol{Z}^H$, where $\boldsymbol{S}$ and $\boldsymbol{T}$ are upper triangular. The eigenvalues are then obtained from the ratio of the diagonal elements of the $\boldsymbol{S}$ and $\boldsymbol{T}$ operators, with $\sigma_j=S_{j,j}/T_{j,j}$ (Golub & Van Loan 1996).

The DNS results in figures 2 and 3 showed that the parameter combination $T=200$ and $W_0=0.40$ causes rapid breakdown to turbulence. The perturbation growth which precedes breakdown takes place at $Re\equiv U_\infty\delta(x)/\nu\approx1600$. The following linear analyses are therefore reported for this particular set of base-flow parameters and Reynolds number. It is important to note that pure Blasius flow at $Re=1600$ is only slightly supercritical and therefore has a very weak Tollmien–Schlichting instability. In addition, a pure Stokes boundary layer at $Re_{Stokes}=90.23$ considered herein is substantially below the critical condition for global instability. The three-dimensional flow over a spanwise oscillating plate may nonetheless show a fundamentally different stability behaviour.

The linear stability analysis is performed for the combined Blasius–Stokes base flow and the average growth rate,

$$\sigma_{i,avg}(\alpha,\beta)\equiv\int_0^1\sigma_i(\alpha,\beta,t/T)\,\mathrm{d}(t/T), \tag{3.11}$$

is evaluated. This quantity provides the net amplification of perturbations over a full period of the base state, and can thus be interpreted as a global measure of disturbance growth. Figure 7 shows $\sigma_{i,avg}$ as a function of the streamwise and spanwise wavenumbers. At the investigated Reynolds number, the global maximum of $\sigma_{i,avg}$ is nearly zero, and hence all modes are stable in an average sense. Two distinct regions exist where $\sigma_{i,avg}$ is least negative. The local maximum around $(\alpha,\beta)=(0.8, 0.0)$ is due to the classical Tollmien–Schlichting wave that is also found in pure Blasius boundary layers. The second region of positive growth at $(\alpha,\beta)\approx(0.8, 1.4)$ relates to an instability specific to the Blasius–Stokes boundary layer. However, its very weak growth rate when averaged over a period of the base flow does not explain the rapid breakdown observed in the simulations. One possible

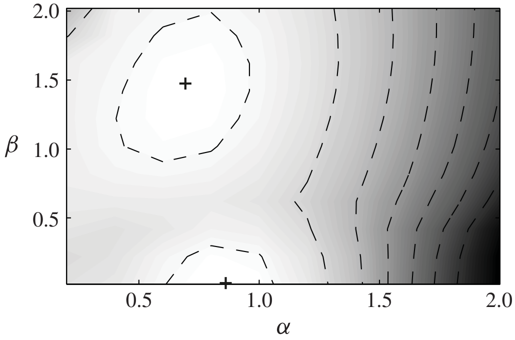

FIGURE 7. Contours of the averaged growth rate $-0.12 \leqslant \sigma_{i,avg} \leqslant 0.00$ at $Re = 1600$. Symbols mark the local maxima.

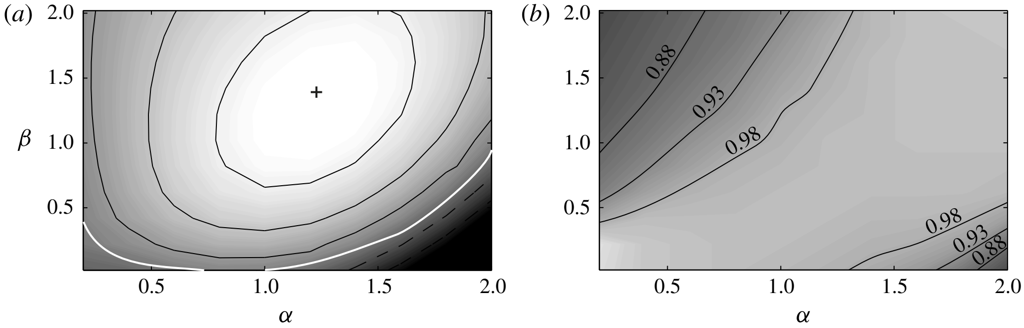

FIGURE 8. (a) Contours of the maximum growth rate, $-0.04 \leqslant \sigma_{i,max} \leqslant 0.04$. The cross marks the maximum and the white line is the neutral curve. The symbol marks the global maximum. (b) Contours of the most unstable phase $0.7 \leqslant (t/T)_{max} \leqslant 1.1$.

rationale is that the instability in the DNS is associated with modes that undergo rapid growth during short fractions of the base-flow period, but their average growth rate over an entire period is small. In order to examine this hypothesis, figure 8 shows the modal growth rate maximized over all phases,

$$\sigma_{i,max}(\alpha, \beta) \equiv \max_{t/T} \sigma_i(\alpha, \beta, t/T) \tag{3.12}$$

as a function of the streamwise and spanwise modal wavenumbers at $Re = 1600$. The maximum growth rate is recorded at the wavenumber pair $(\alpha, \beta) = (1.2, 1.4)$. In terms of the inlet boundary layer thickness, the maximum growth rate is observed at $(\alpha_0, \beta_0) = (0.6, 0.7)$, which is similar to the wavenumbers of the most energetic perturbations in the DNS flow field (see figure 4b). The particular phase of the base flow where the highest modal growth rate was recorded is presented in figure 8(b). The contours indicate that the most unstable phase only weakly depends on α and β. The phase of the maximum amplification is $(t/T)_{max} \in [0.82, 1.05]$ for all investigated wavenumber pairs.

The growth rate of the most unstable discrete mode is shown in figure 9(a) as a function of the phase of the base flow during two periods, $t/T = [-0.5, 1.5]$. The figure also includes results for the pure Blasius and pure Stokes boundary layers

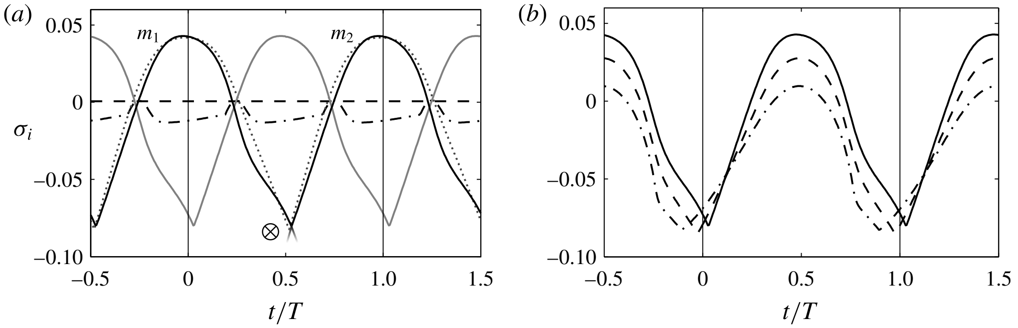

FIGURE 9. Instantaneous temporal growth rate σ_i of the most unstable discrete eigenfunction as a function of the base-flow phase. (*a*) Pure Blasius flow (dashed), pure Stokes layer with $W_0 = 0.40$ (dash-dotted) and combined Blasius–Stokes boundary layer taken from DNS (solid). For comparison, the growth rate for the analytical Blasius–Stokes profile is also included (dotted). Modes corresponding to $(\alpha, \beta) = (1.2, 1.4)$ (black) and $(\alpha, \beta) = (1.2, -1.4)$ (grey). (*b*) Combined Blasius–Stokes boundary layer with forcing parameters $T = 200$ and $W_0 = 0.15$ (dash-dotted), $W_0 = 0.25$ (dashed), $W_0 = 0.40$ (solid) for wavenumbers $(\alpha, \beta) = (1.2, 1.4)$.

for comparison with the combined Blasius–Stokes flow. In each of the three cases, a complete sweep of the (α, β) plane was conducted. The presented growth rates therefore correspond to the respective most unstable wavenumber combinations for each base flow. For pure Blasius flow, the corresponding values are $(\alpha, \beta) = (0.9, 0)$. The flow is known to become unstable at $Re \approx 1500$, and the present Reynolds number of 1600 therefore yields a small positive growth rate for the Tollmien–Schlichting wave. When considering the case of a pure Stokes flow, the Reynolds number based on the Stokes layer is $Re_{Stokes} = 90.23$ and thus substantially below the critical value, $Re_{Stokes} = 708$, for which the flow becomes globally unstable. In agreement with this observation, the growth rate which was evaluated at $(\alpha, \beta) = (0.0, 3.0)$ remains negative for the largest part of the forcing period, except for two very short intervals during which a marginally positive σ_i is recorded. Finally, a superposition of the Blasius profile and the transverse Stokes layer is examined for the wavenumber pair $(\alpha, \beta) = (1.2, 1.4)$. A substantial variation in the growth rate is observed. The maximum growth rate, which occurs at $t/T \approx 0$, exceeds that of the TS wave by two orders of magnitude. A significant stabilization half a period later compensates for this growth and, as a result, the time-averaged growth rate over a full period is approximately zero. The grey line is the maximum growth rate evaluated at $(\alpha, \beta) = (1.2, -1.4)$. The results simply appear shifted in phase due to the symmetry of the wall motion. The substantial change in the instability characteristics arising from the superposition of the Stokes and Blasius layers is akin to the problem of streamwise oscillating channel flow, which was shown by Thomas *et al.* (2011) to be highly sensitive to the addition of a steady mean component. The influence of the wall-oscillation amplitude on modal stability is visualized in figure 9(*b*). It is seen that both the maximum growth rate and the extent of the unstable interval increase with W_0.

For the present range of parameters, the Stokes layer alone is only weakly unstable at certain phases, and it is the superposition with the Blasius profile that substantially promotes modal growth (figure 9*a*). The instability analysis is repeated in the limit $Re \to \infty$ to assess whether the amplification is due to an inviscid mechanism. The

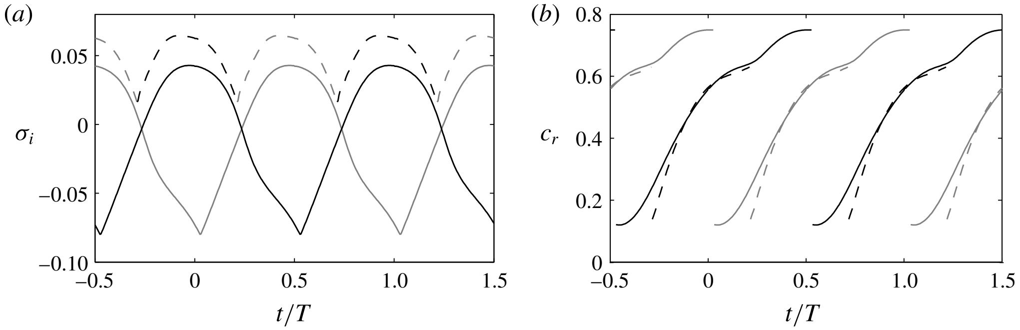

FIGURE 10. (*a*) Temporal growth rate σ_i of the instantaneously most unstable discrete mode at $Re = 1600$ (solid) and in the inviscid limit $Re \rightarrow \infty$ (dashed). (*b*) Phase speed c_r of the instantaneously most unstable discrete mode at $Re = 1600$ (solid) and in the inviscid limit (dashed). Modes corresponding to $(\alpha, \beta) = (1.2, 1.4)$ (black) and $(\alpha, \beta) = (1.2, -1.4)$ (grey).

maximum growth rates of the inviscid modes with $(\alpha, \beta) = (1.2, 1.4)$ and $(\alpha, \beta) = (1.2, -1.4)$ are presented by dashed lines in figure 10(*a*). The behaviour qualitatively agrees with the analysis performed at $Re = 1600$, although higher growth rates are observed in the absence of viscosity. The phase speeds of both the viscous and the inviscid modes are presented in figure 10(*b*). The results show that the discontinuity in σ_i of the viscous modes is accompanied by a jump in c_r that is also present in the inviscid limit. Overall, these findings establish that the modal instability is due to an inviscid mechanism. As such, the present instability bears a certain resemblance to the cross-flow instabilities that arise in the three-dimensional flow over swept wings.

3.3. *Mode crossing and its origin*

In this section, we examine the origin of the abrupt change in the slope of the instability growth rate, marked by the '$\otimes$' in figure 9. Note that we are considering only the curve for $(\alpha, \beta) = (1.2, 1.4)$ in that figure, and not the $(\alpha, -\beta)$ result. The sudden change in the trend of σ_i can be attributed to a crossing of two discrete modes. While σ_i may appear periodic over a period T of the base flow in that figure, the mode crossing indicates otherwise. In particular, the mode with the highest growth rate at $t/T = 0$ (labelled m_1) is not the same as the dominant mode (m_2) at $t/T = 1$. The mode crossing is also evident in the eigenfunctions of the instantaneously most unstable mode (figure 11). The eigenfunctions at $t/T = 0.50$ and $t/T = 0.54$ provide a comparison immediately before and after the crossing, and show an appreciable shift of the location of highest amplitude towards the wall.

In order to further examine the periodic behaviour of the discrete instabilities, a series of eigenvalue problems at different phases of the base state are solved. A particular eigenvalue can then be traced in the complex plane either to earlier or later phases of the base flow. This process is termed the backward and forward continuation of the eigenvalue of interest. Figure 12 shows the backward and forward continuations of the modes which are most unstable at phases $t/T = k$, $t/T = k + 1$ and $t/T = k + 2$. The interval over which each of the modes remains the most unstable is marked by a solid line. The aforementioned mode crossing is observed at approximately $t/T = k + 0.52$. It is further seen that, at each time instance, the system contains a multiplicity of discrete modes: the most unstable eigenfunction, and the modes that will become unstable during the following periods exist simultaneously.

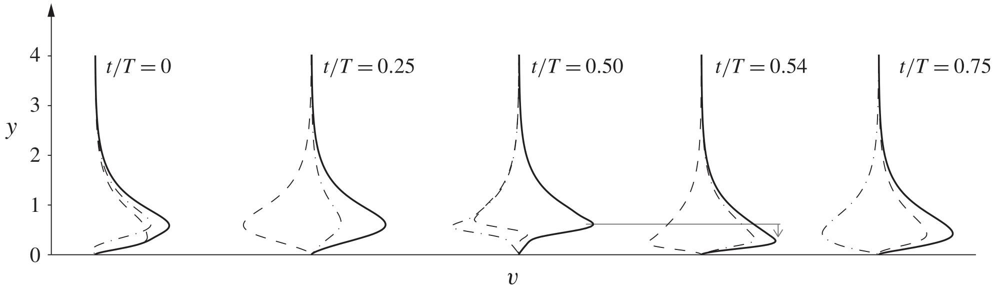

FIGURE 11. Absolute (solid), real (dashed) and imaginary (dash-dotted) components of the instantaneously most unstable mode at different phases of the base flow.

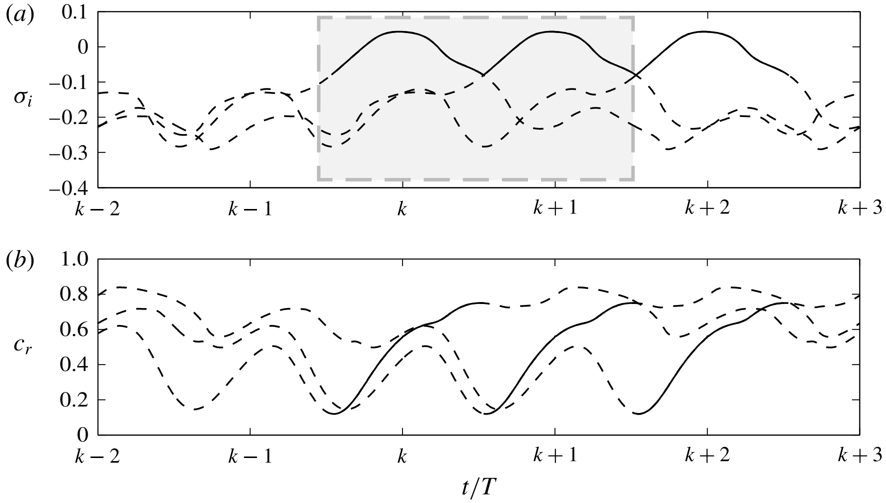

FIGURE 12. Continuation of discrete modes over several forcing periods. (*a*) Temporal growth rate. (*b*) Phase speed. The interval for which the mode becomes the most unstable eigenfunction is marked by a solid line.

The mode crossing can be attributed to the character of the Stokes layer. Figure 13(*a*) shows that contours of the time-dependent spanwise base flow are aligned at a characteristic angle in the $(y, t/T)$-plane. This angle represents the group velocity $c_g \sim \sqrt{\nu T}$ of Stokes second problem, which also governs the wall-normal propagation of the inflection points $\mathscr{D}^2 W = 0$ generated by the Stokes layer. The dashed lines in figure 13(*b*), which give the y-coordinate of the inflection point closest to the wall as a function of t/T, is therefore aligned at the same angle as the contours in figure 13(*a*).

The propagation of the inflection points is related to the instability modes from figure 12 by including the height of their critical layers in figure 13(*b*). The mode crossing at $t/T = k + 0.52$ coincides with the emergence of a new inflection point at the wall. As the inflection point travels away from the wall, it draws along the mode, which in the process becomes more unstable. When the next inflection point is generated one period later, the previously most unstable mode is at the edge of the boundary layer. The new inflection point thus attracts a different eigenfunction situated closer to the wall.

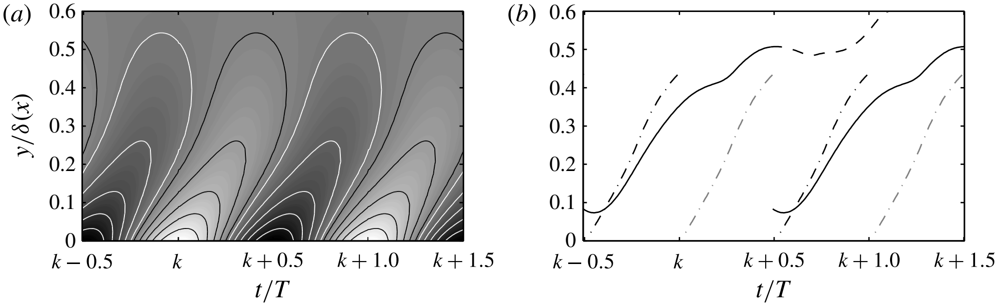

FIGURE 13. (*a*) Contours of the spanwise velocity component computed in DNS as a function of base-flow phase t/T and wall distance y. (*b*) Wall distance of the first inflection point of the spanwise velocity profile (dash-dotted). Wall distance of the critical layer of the most unstable eigenfunctions for $(\alpha, \beta) = (1.2, 1.4)$ (solid).

It is important to note that thus far the focus was on the wavenumber pair (α, β) that is most unstable due to one inflection point of the base flow, and which repeats once every period. However, the Stokes layer also generates a second inflection point within the period, or more precisely half a period out of phase. This second inflection point induces a similar trend, but at the wavenumber pair $(\alpha, -\beta)$ – the grey curve in figure 9(*a*).

The discussion has to this point relied on stability analyses of instantaneous phases of the base state. A Floquet analysis, on the other hand, would take into account the time-harmonic nature of the base flow and identify the eigenmodes with maximum amplification over the entire period. A comparison of the two approaches is provided in appendix A. The most unstable Floquet mode is fundamental, i.e. its period matches the base flow. Its growth rate is, however, significantly lower than the average growth rate, $\sigma_{i,avg}$, of the instantaneous mode at the wavenumber pair $(\alpha, \beta) = (1.2, 1.4)$ where $\sigma_{i,avg}$ is maximum.

The analysis of the instantaneously most unstable phases highlights the propensity of these inflection points of the spanwise profile to cause significant energy amplification during parts of the base-flow cycle. This behaviour is compared to the perturbation field in the DNS of transition to turbulence in the next section.

3.4. *Comparison to DNS*

In the following, we examine whether results from instantaneous stability analysis can explain the strongly phase-dependent perturbation field observed in direct numerical simulations of transition. The focus is again on the wavenumber pair $(\alpha_0, \beta_0) = (0.6, 0.7)$, which is subject to the highest instantaneous growth for the examined range of Reynolds numbers. The modal growth rate as a function of the phase of the base flow and the downstream location is provided in figure 14(*a*). The growth rate increases throughout the forcing period with x, while the most unstable phase is shifted by approximately one quarter of a period from $(t/T)_{max} \approx 0.90$ at $x \approx 50$ to $(t/T)_{max} \approx 0.15$ at $x \approx 200$.

An attempt is made to relate the disturbance field from direct numerical simulations and the results from the linear stability analyses by integrating the modal growth rate in time. While an instability mode in the DNS is convected downstream as it amplifies, the instability analysis only provides a purely temporal growth rate for

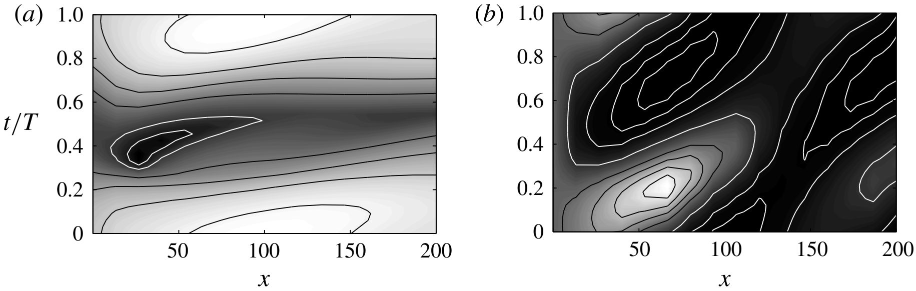

FIGURE 14. (*a*) Contours of the instantaneous temporal growth rate of the most unstable discrete mode $-0.12 \leqslant \sigma_i \leqslant 0.05$. (*b*) Contours of the integrated growth rate of the most unstable discrete mode $0.0 \leqslant \Sigma_i \leqslant 2.5$.

a given Reynolds number and as such a particular downstream position. In order to incorporate this simultaneous change of both time and space, the integration is performed along rays of constant characteristic speed $c_c = 0.60$, taken from the angle in the phase-averaged space–time diagram (figure 5). The integrated growth rate is therefore defined as

$$\Sigma_i(t, x) \equiv \int_{t-x/c_c}^{t} \sigma_i(x - c_c t, t)\,\mathrm{d}t. \tag{3.13}$$

Evaluation of Σ_i for all possible phases as well as for a range of downstream positions yields the two-dimensional data field presented in figure 14(*b*). Localized regions in which Σ_i is larger and smaller than zero are identified, corresponding to locations where the integral effect of exponential amplification is growth and decay, respectively.

A comparison of the integrated growth rate with the perturbation level observed in DNS is provided in figure 15 at three different downstream positions. The dashed and dash-dotted lines correspond to normalized streamwise and wall-normal velocity fluctuations in the simulations at $y/\delta(x) = 0.30$. Different wall distances yield similar results. The integrated growth rate Σ_i is reported at three downstream positions, normalized to a unit peak value (solid lines). Black and grey curves correspond to modes with wavenumbers $(\alpha_0, \beta_0) = (0.6, 0.7)$ and $(\alpha_0, \beta_0) = (0.6, -0.7)$, respectively. The occurrence of two peaks per period in the DNS fluctuation level is explained by the presence of both $(\alpha, \pm\beta)$ perturbations in the broadband disturbance field inside the boundary layer.

3.5. *Influence of Re and Re_{Stokes}*

The streamwise Blasius boundary layer and the spanwise Stokes layer introduce two independent Reynolds numbers, $Re = U_\infty \delta/\nu$ and $Re_{Stokes} = W_0\sqrt{T/\pi\nu}$. In order to establish their respective significance for perturbation growth in the present three-dimensional base state, figure 16 provides the maximum instantaneous modal growth rate as a function of the period and the amplitude of the wall forcing,

$$\sigma_{i,peak}(T, W_0) \equiv \max_{t/T} \max_{\alpha} \max_{\beta} \sigma_i(\alpha, \beta, t/T, T; W_0). \tag{3.14}$$

Dotted black lines are isolevels of the growth rate, and solid white lines mark contour lines of the Reynolds number of the Stokes layer. The curves are locally not

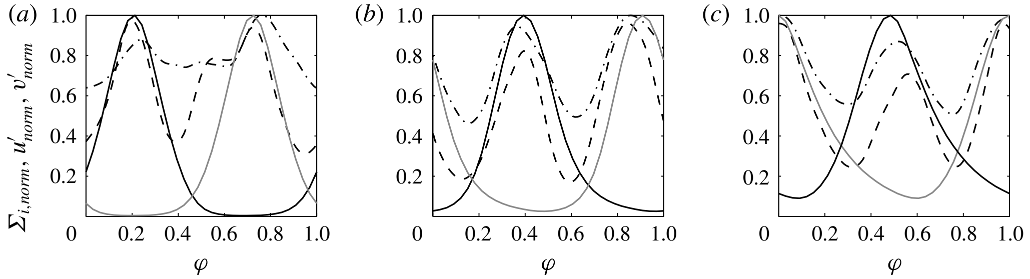

FIGURE 15. Integrated growth rate Σ_i for modes $(\alpha_0, \beta_0) = (0.6, 0.7)$ (solid black) and $(0.6, -0.7)$ (solid grey) and the velocity fluctuations $\langle |u| \rangle_\varphi$ (dashed) and $\langle |v| \rangle_\varphi$ (dash-dotted) observed in DNS. From (*a–c*): $Re = 1400$, $Re = 1600$ and $Re = 1800$.

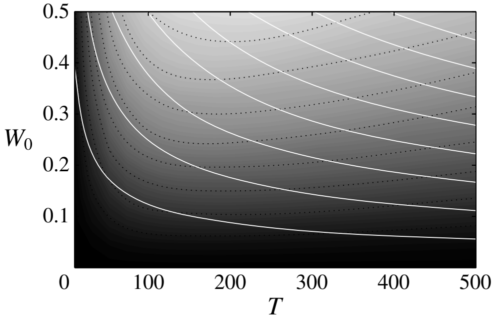

FIGURE 16. Grey contours and dotted black lines: maximum modal growth rate from $\sigma_{i,peak} = 0$ (black) to $\sigma_{i,peak} = 0.04$ (white) in increments of 4×10^{-3}. Solid white lines mark levels of constant Re_{Stokes} from 0 to 175 in increments of 25.

parallel and, therefore, the growth rate is not determined solely by Re_{Stokes}. While higher forcing amplitudes W_0 induce higher growth rates, there exists a specific period T_{max} for which modal growth is highest. The dependence of this period on the downstream Reynolds number, $Re = U\delta(x)/\nu$, is shown in figure 17(*a*). The period remains independent of W_0 but increases with Re. Figure 17(*b*) depicts the ratio of the thickness of the Stokes layer corresponding to T_{max} and the Blasius boundary layer thickness, $\delta_{Stokes,max}/\delta(x)$. This ratio remains nearly constant as the Reynolds number increases from 800 to 2800.

This section has focused on the modal instability which can promote disturbance growth when spanwise wall oscillation is superimposed on a streamwise Blasius boundary layer. However, for a judicious choice of parameters, wall actuation can also effectively delay bypass transition (see figure 2*b*) – an effect which is examined in detail in § 4.

4. Non-modal growth

In this section, the effect of spanwise wall forcing on the non-modal lift-up mechanism that causes the formation of boundary layer streaks is evaluated. The main objective is to explain the weaker perturbation field which is observed in figure 2(*b*). After a summary of DNS results, linear optimal growth analysis is employed in order to explain the observed behaviour.

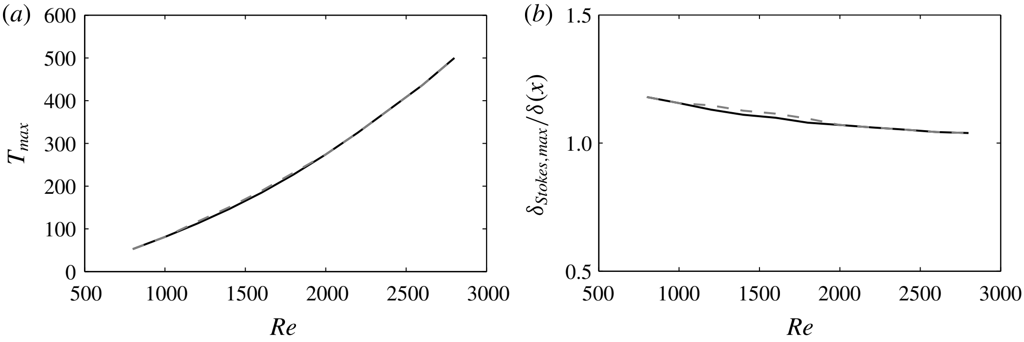

FIGURE 17. (*a*) Most unstable forcing period T_{max} for amplitudes $W_0 = 0.25$ (grey dashed) and $W_0 = 0.40$ (solid black) as a function of the downstream Reynolds number, $Re = U\delta(x)/\nu$. (*b*) Ratio $\delta_{Stokes,max}/\delta$ of the thickness of the Stokes layer corresponding to the locally most unstable period T_{max} and the local boundary layer thickness as a function of the downstream Reynolds number, $Re = U\delta(x)/\nu$.

4.1. *Streaks in DNS*

It is instructive to start with an analysis of conditionally sampled DNS flow fields. During the simulations, a sequence of instantaneous three-dimensional flow fields $\boldsymbol{u}_{DNS}(x, y, z, t) = (u(x, y, z, t), v(x, y, z, t), w(x, y, z, t))^{\mathrm{T}}_{DNS}$ was stored. Laminar–turbulent discrimination is applied to each of the flow fields. Within the laminar regime, the streaks are identified and their properties are extracted using the procedure described by Nolan & Zaki (2013). The outcome is a database that contains the three-dimensional coordinates and the amplitudes for all the detected streaks at each time step. The conditionally averaged fluctuation field at a given downstream position x and phase φ is then defined as

$$\{\boldsymbol{u}'\}_{\pm}(x, y, \tilde{z}, \varphi) \equiv \frac{1}{N_{\pm}} \sum_{n=1}^{N_{\pm}} \boldsymbol{G}(z_{n\pm})\boldsymbol{u}'(x, y, z_{n\pm}, \varphi), \tag{4.1}$$

where indices '+' and '−' denote high- and low-speed streaks, respectively. The linear operator $\boldsymbol{G}(z_{n\pm})$ translates the averaging window in the span in order to align the spanwise location of the maximum streak amplitude at $\tilde{z} = 0$.

For a reference simulation in the absence of wall forcing, figure 18 shows conditionally sampled high-speed and low-speed streaks. The downstream position is $x = 170$, and the average is computed from a total of 7672 (9114) individual high-speed (low-speed) streaks. The respective peak magnitudes of the conditional averages of both types of streaks are $\max(|\{u'\}_+|) = 0.1064$ and $\max(|\{u'\}_-|) = 0.0937$.

The conditional averaging was also applied to flow fields computed in the presence of the wall oscillation with optimal forcing parameters ($W_0 = 0.25$, $T = 200$). Figure 19 depicts the averages of positive and negative boundary layer streaks at four phases, which are equally distributed over half a period of the wall-oscillation cycle. At the first phase, the appearance of the conditionally averaged streaks is similar to the unforced reference case (figure 18). The peak magnitudes of high-speed ($\max(|\{u'\}_+|) = 0.0456$) and low-speed streaks ($\max(|\{u'\}_-|) = 0.0424$) are nevertheless substantially smaller. Moreover, the peak magnitude is located at a higher wall distance than in the absence of the spanwise base-flow component. In

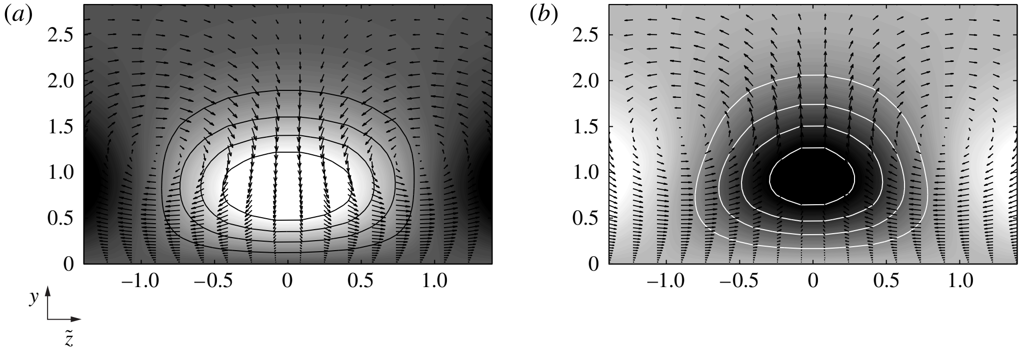

FIGURE 18. Conditionally averaged streaks from an unforced reference simulation at downstream position $x=140$. Grey contours and solid lines show $\{u'\}_\pm$, vectors indicate $\{v'\}_\pm$ and $\{w'\}_\pm$. High-speed streaks (*a*) and low-speed streaks (*b*).

figure 19(*c*,*d*) ($\varphi = 0.125$), both types of streaks reach their highest amplitudes. In addition, the spanwise base flow causes a substantial deformation of the portion of the streaks closest to the wall. Immediately afterwards, the streaks weaken considerably (figure 19*e*,*f*). The last row shows a further reduction of the streak amplitudes.

In order to explain this substantial reduction of streak amplitudes in the presence of the spanwise wall motion, the non-modal mechanism that causes their formation is examined using optimal disturbance analysis.

4.2. *Optimal disturbance analysis*

The methodology for computing the optimally amplified initial condition for the present time-dependent flow is based on the iteration of the forward and adjoint governing equations (Schmid 2007). Similar to the modal analyses presented in § 3, here too the base state is computed from laminar-flow simulations without any free-stream turbulence. The triple decomposition of the instantaneous flow field (2.1) hence reduces to $u=\bar{u}$ and $w=\tilde{w}_\varphi$, which is again referred to as a Blasius–Stokes flow.

The time evolution of small perturbations in v' and $\eta' = (\partial u'/\partial z) - (\partial w'/\partial x)$ can be expressed in terms of a linear initial value problem. A normal-mode ansatz is applied for the streamwise and spanwise dimensions,

$$v' = v(y, t)\exp(\mathrm{i}(\alpha x + \beta z)) \tag{4.2}$$

$$\eta' = \eta(y, t)\exp(\mathrm{i}(\alpha x + \beta z)). \tag{4.3}$$

Furthermore, let $\boldsymbol{q} = (v, \eta)^{\mathrm{T}}$, then the governing equations for small perturbations can be written in operator form,

$$\left(\boldsymbol{L} - \boldsymbol{M}\frac{\partial}{\partial t}\right)\boldsymbol{q} = 0, \tag{4.4}$$

with the definitions of $\boldsymbol{L}$ and $\boldsymbol{M}$ provided in § B.1. The fundamental solution operator $\boldsymbol{A}$ describes the time integration of (4.4) from the initial time, t_0, to the final time, t_1, so that

$$\boldsymbol{q}_1 = \boldsymbol{A}\boldsymbol{q}_0. \tag{4.5}$$

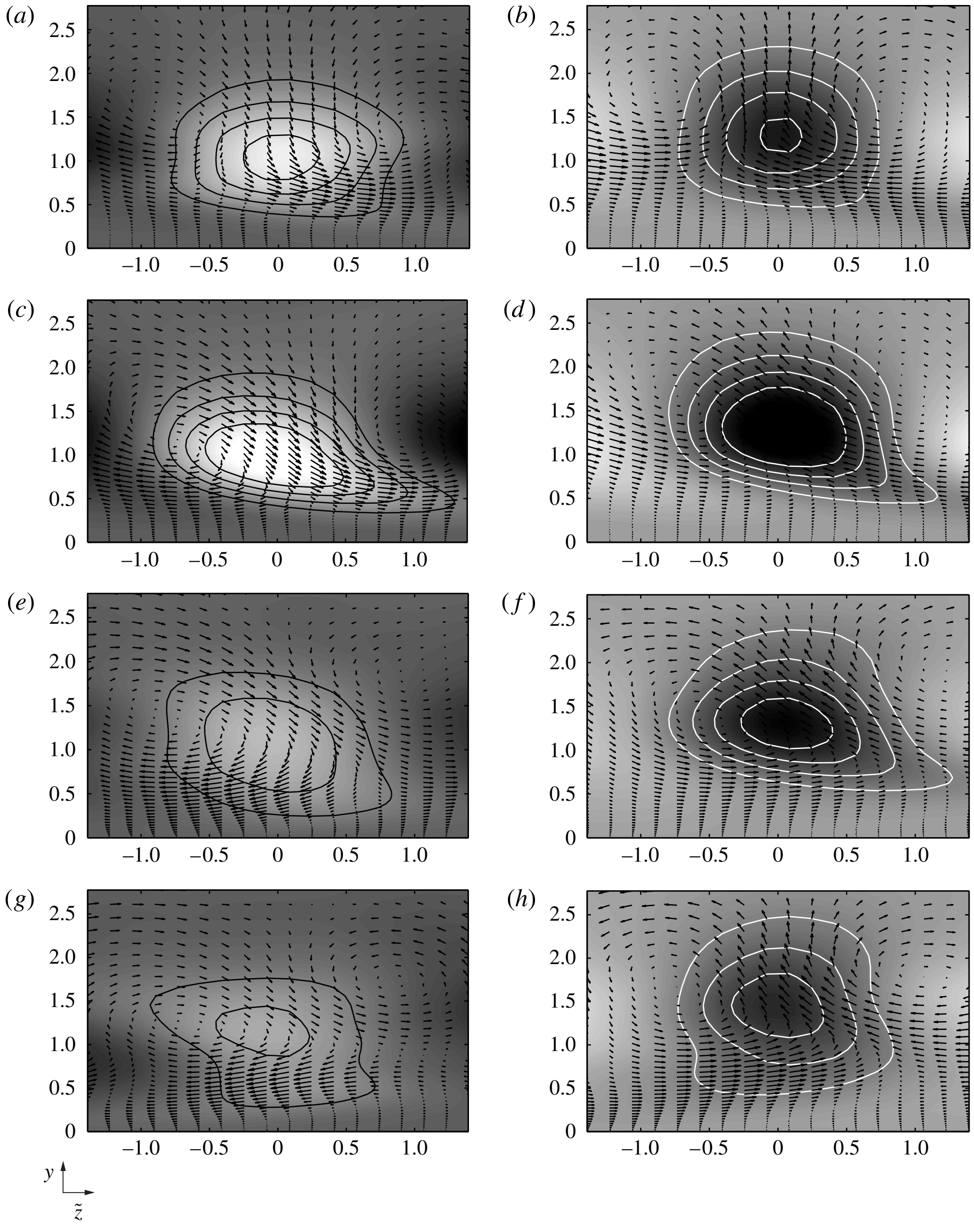

FIGURE 19. Conditionally averaged streaks from simulations with $T = 200$, $W_0 = 0.25$ at downstream position $x = 140$ and phases $\varphi = \{0, 0.125, 0.250, 0.375\}$ in (*a*,*b*), (*c*,*d*), (*e*,*f*), (*g*,*h*) respectively. The background colour and solid lines show $\{u'\}_\pm$. Vectors represent $\{v'\}_\pm$ and $\{w'\}_\pm$. High-speed streaks (*a*,*c*,*e*,*g*) and low-speed streaks (*b*,*d*,*f*,*h*).

For an arbitrary state vector $\boldsymbol{q}$, the kinetic energy within the domain Ω_y is given by the norm

$$(\boldsymbol{q}, \boldsymbol{q})_E \equiv \int_{\Omega_y} \boldsymbol{q}^H \boldsymbol{Q} \boldsymbol{q} \, \mathrm{d}y, \tag{4.6}$$

where

$$\boldsymbol{Q}=\begin{bmatrix} k^2-\mathscr{D}^2 & 0 \\ 0 & 1 \end{bmatrix}. \tag{4.7}$$

Finding an optimally amplified initial condition $\boldsymbol{q}_0$ is then equivalent to maximizing the functional

$$J(\boldsymbol{q})=\frac{(\boldsymbol{q}_1,\boldsymbol{q}_1)_E}{(\boldsymbol{q}_0,\boldsymbol{q}_0)_E}=\frac{(\boldsymbol{A}\boldsymbol{q}_0,\boldsymbol{A}\boldsymbol{q}_0)_E}{(\boldsymbol{q}_0,\boldsymbol{q}_0)_E}=\frac{(\boldsymbol{q}_0,\boldsymbol{A}^{\dagger}\boldsymbol{A}\boldsymbol{q}_0)_E}{(\boldsymbol{q}_0,\boldsymbol{q}_0)_E}. \tag{4.8}$$

The adjoint fundamental solution operator $\boldsymbol{A}^{\dagger}$ introduced in the last line formally describes the time integration of the adjoint governing equations,

$$\left(\boldsymbol{L}^{\dagger}-\boldsymbol{M}^{\dagger}\frac{\partial}{\partial t}\right)\boldsymbol{q}^{\dagger}=0, \tag{4.9}$$

from t_1 to t_0 with the definitions of $\boldsymbol{L}^{\dagger}$ and $\boldsymbol{M}^{\dagger}$ given in § B.2. The last term in (4.8) is a Rayleigh quotient, and the optimal energy-amplification ratio, G, is therefore given by the primary eigenvalue, λ_{max}, of the product $\boldsymbol{A}^{\dagger}\boldsymbol{A}$, i.e. $G\equiv\max_{\boldsymbol{q}_0} J(\boldsymbol{q})=\lambda_{max}$. Computation of λ_{max} via simple power iteration involves the repeated application of $\boldsymbol{A}^{\dagger}\boldsymbol{A}$ to a random initial guess. The matching conditions between $\boldsymbol{q}$ and $\boldsymbol{q}^{\dagger}$ are

$$\text{Forward} \rightarrow \text{Adjoint:} \qquad v_1^{\dagger}=-v_1 \qquad \eta_1^{\dagger}=\eta_1 \tag{4.10}$$

$$\text{Adjoint} \rightarrow \text{Forward:} \qquad v_0=-\frac{v_0^{\dagger}}{(\boldsymbol{q}_1,\boldsymbol{q}_1)_E} \qquad \eta_0=\frac{\eta_0^{\dagger}}{(\boldsymbol{q}_1,\boldsymbol{q}_1)_E}. \tag{4.11}$$

In addition, the initial condition is normalized to unit energy, i.e. $E_0\equiv(\boldsymbol{q}_0,\boldsymbol{q}_0)_E\equiv 1$.

The efficiency of the computation of λ_{max} is improved by replacing the power iteration with an Arnoldi scheme. In this case, the solutions $\boldsymbol{q}_0^{\dagger}$ obtained at the end of each cycle are orthogonalized and used to construct a Krylov subspace, see e.g. Golub & Van Loan (1996). A spectral discretization using Chebyshev polynomials is employed in the wall-normal dimension. The mapping between the computational and physical domain is chosen such that half of the 320 Gauss–Lobatto points of the spectral grid are located within the boundary layer. The domain height is ten local boundary layer thicknesses, $y\in[0, 10\delta]$, and homogeneous boundary conditions are adopted at the wall as well as at the top of the numerical domain. An implicit second-order backward discretization is used for the time integration of the both the forward and the adjoint problems. The state vector at time step $k+1$ is therefore obtained from solving the linear system

$$(3\boldsymbol{M}-2\Delta t\boldsymbol{L}^{k+1})\boldsymbol{q}^{k+1}=\boldsymbol{M}(4\boldsymbol{q}^{k}-\boldsymbol{q}^{k-1}). \tag{4.12}$$

Since the reference Blasius case has a steady base state, the maximum amplification only depends on the duration between the initial and final times t_1-t_0. For unsteady base states, the initial time, t_0, and the final time, t_1, of the optimization are independent parameters. As such, the optimization procedure can be applied in one of two perspectives: the first is to consider the initial phase, φ_0, as a parameter. The final time, t_1, is then varied in order to identify the most highly amplified disturbances for each φ_0. The second perspective is that the flow can only be at one of a set of final phases (Blesbois *et al.* 2013). For each of these final phases, φ_1, the optimization is performed for all possible initial times (figure 20). While the

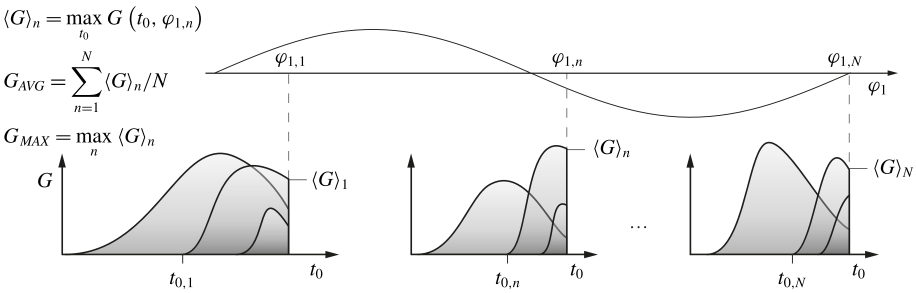

FIGURE 20. Schematic of the optimization of perturbation kinetic energy for a prescribed target phase φ_1 over all possible initial times t_0.

two approaches explore the same parameter space, the interpretation is different. In particular, the second approach, which is adopted here, yields the most amplified, or most likely observed disturbance at any (final) phase of the flow and identifies its starting point earlier in time,

$$\langle G\rangle_n \equiv \max_{t_0} G(t_0, \varphi_{1,n}). \tag{4.13}$$

With this in mind, one can also evaluate the average energy-amplification ratio over these possible final phases,

$$G_{AVG} \equiv \frac{1}{N}\sum_{n=1}^{N} \langle G\rangle_n, \tag{4.14}$$

and the global optimum,

$$G_{MAX} \equiv \max_n \langle G\rangle_n. \tag{4.15}$$

4.3. *Results*

This section presents a set of key results of algebraic energy growth in the presence of the spanwise wall forcing. The focus is on streamwise elongated perturbations with $\alpha = 0$. The influence of a number of parameters such as the period and amplitude of the wall forcing, the Reynolds number and the spanwise length scale of the disturbance is investigated.

A comparison of algebraic energy growth without and with application of the spanwise wall motion is presented in figure 21. Panel 21(*a*) provides $G_{AVG} = G_{MAX}$ for a pure Blasius boundary layer. In agreement with the literature, the highest amplification occurs for spanwise wavenumber $\beta \approx 2$. The value of G_{AVG} in the forced case with parameters $W_0 = 0.25$ and $T = 200$ is presented in figure 21(*b*), where G_{AVG} is substantially smaller than for the pure Blasius flow.

The influence of the Reynolds number on non-modal growth is presented in figure 22. At each *Re*, the particular β that yields the highest growth is considered. For Blasius flow, the energy gain shows the established quadratic dependence on *Re* (Butler & Farrell 1992). In the presence of the wall motion, the increase of G with *Re* is less pronounced, and the relative difference between the unforced and forced cases grows with *Re*.

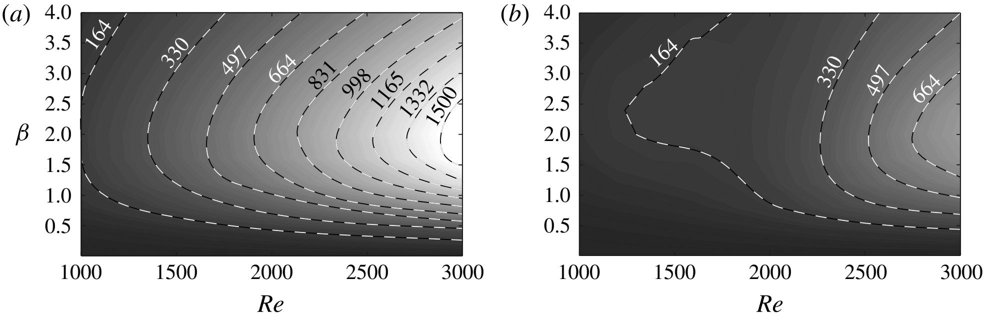

FIGURE 21. Averaged energy-amplification ratio, $0 \leqslant G_{AVG} \leqslant 1500$. (*a*) Pure Blasius. (*b*) Forcing with $T = 200$, $W_0 = 0.25$.

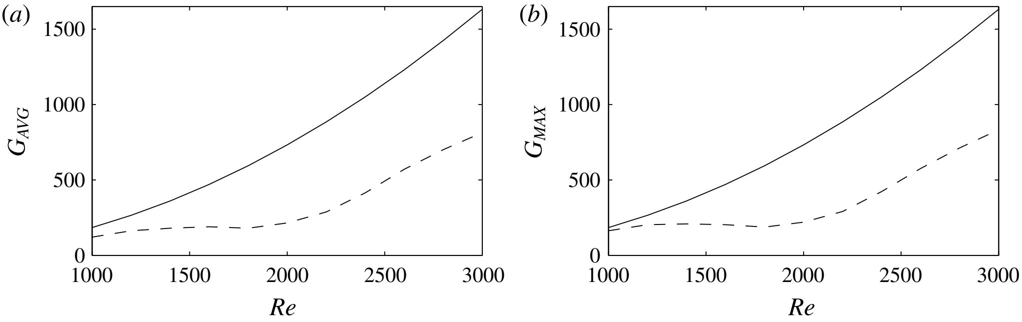

FIGURE 22. Energy amplification for Blasius (solid), sinusoidal forcing with $T = 200$, $W_0 = 0.25$ (dashed) for the highest amplified spanwise wavenumber β over Reynolds number. (*a*) Averaged energy-amplification ratio G_{AVG}. (*b*) Maximum energy-amplification ratio G_{MAX}.

The phase dependence of the non-modal growth process is visualized in figure 23. Panel 23(*a*) shows the optimization of the energy gain over all initial times for the target ending phase $\varphi_1 = 0.125$. This particular ending phase is host to the global maximum, G_{MAX}. An appreciable influence of the initial time of the optimization procedure is observed. Perturbations which start to grow at approximately $t_0/T = -0.4 \pm k/2,\ k \in \mathbb{N}$ are higher amplified than those starting to grow at other times. This bias towards certain initial times is even more evident in figure 23(*b*). For a range of equidistant ending phases $\varphi_1 \in [0, 1]$, the time evolution of the energy $E = (\boldsymbol{q}, \boldsymbol{q})_E$ of the initial disturbance that yields the highest G is shown. In agreement with the above observation, all curves start at $t_0/T = -0.4 \pm k/2,\ k \in \mathbb{N}$.

The initial and final conditions yielding the highest G are presented in figure 24. Figure 24(*a*) shows the unforced reference case at initial time. The streamwise velocity component is virtually zero everywhere, while the wall-normal and spanwise components form counter-rotating streamwise vortices. The wall-normal transport of mean momentum induced by these vortices leads to the strong streamwise perturbations observed at the final time. When considering the forced case, the initial condition which yields G_{MAX} consists of streamwise vortices that are tilted in the spanwise direction. As pointed out by Blesbois *et al.* (2013), this characteristic configuration yields an additional non-modal energy gain as the spanwise base-flow

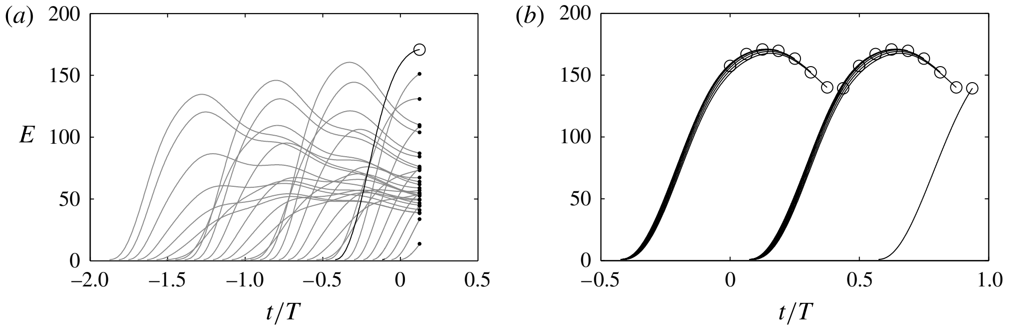

FIGURE 23. Phase dependence of non-modal energy growth for $\beta = 2.00$, $Re = 1800$. (*a*) Energy norm E for a range of initial times t_0/T and ending phase $\varphi_1 = 0.125$. (*b*) Energy norm E for the particular initial times t_0/T that yield the highest energy-amplification ratio G for a set of equidistant ending phases φ_1.

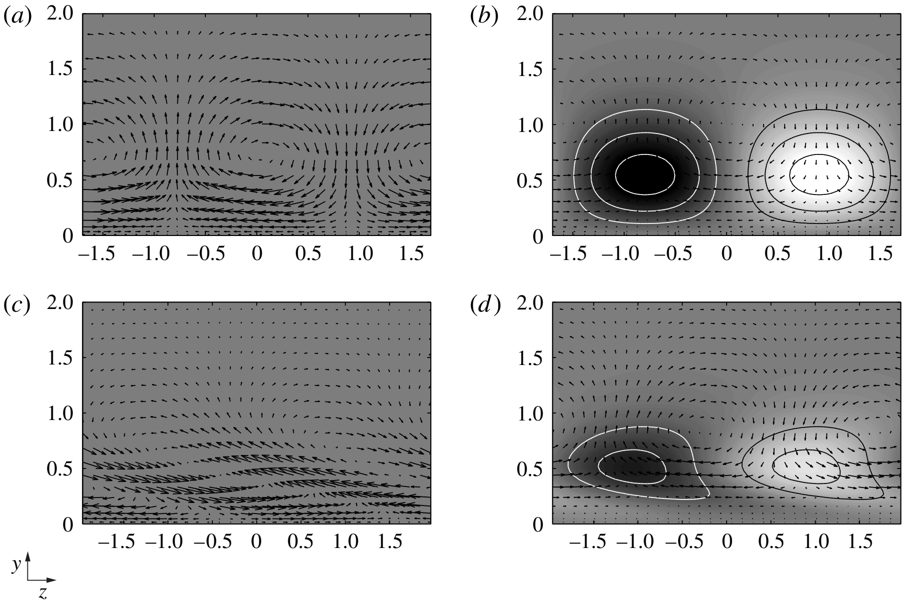

FIGURE 24. Perturbation fields yielding the maximum energy gain G_{MAX}. Flood and line contours give the streamwise velocity component, vectors represent the wall-normal and spanwise velocity components. (*a*,*c*) Initial condition $\boldsymbol{q}_0$ with $E(t_0) \equiv 1$, (*b*,*d*) solution $\boldsymbol{q}(t)$ at final time with $E(t) \equiv G_{MAX}$: (*a*,*b*) pure Blasius, (*c*,*d*) optimal forcing.

component realigns the perturbation field. The configuration of v' and w' at the final phase is very similar to that of the reference case, although the resulting streaks are substantially weaker.

Finally, figure 25 establishes the influence of the period and amplitude of the wall motion on streak growth. For this extensive parameter study, which spans a wide range of T and W_0, the analysis adopts an analytic base-flow profile (a comparison of the analytic and simulated Blasius–Stokes profiles was performed by Hack & Zaki (2014*a*)). Perturbation growth is weakened most effectively at $T \approx 200$. This value

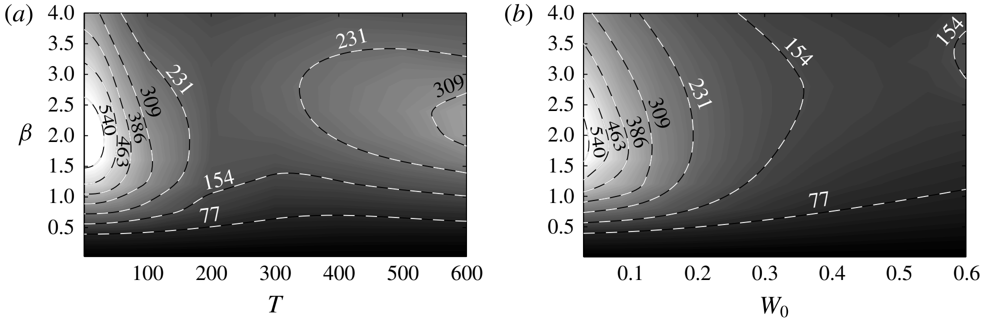

FIGURE 25. Phase-averaged energy-amplification ratio, $0 \leqslant G_{AVG} \leqslant 550$. (*a*) Variation of the forcing period T at $W_0 = 0.25$. (*b*) Variation of the forcing amplitude W_0 at $T = 200$.

coincides with the optimal forcing period established in terms of delaying bypass transition according to the DNS by Hack & Zaki (2014*a*). The influence of the forcing amplitude on the other hand is monotonic, so that higher W_0 increasingly weakens the streak mechanism. This result is further evidence that the early breakdown in the DNS at high W_0 is unrelated to the non-modal growth of boundary layer streaks at $\alpha = 0$.

4.4. *Mechanism of streak weakening*

The optimal growth computations presented above demonstrated a weakening in the maximum possible amplification of streaks in the presence of the wall forcing. In this section, the physical mechanism underlying this behaviour is examined. The optimal initial condition $\boldsymbol{q}_0$ for the pure Blasius boundary layer is advanced in time with the linearized governing equations (4.4). The computed energy norm $E = (\boldsymbol{q}, \boldsymbol{q})_E$ as a function of time is reported in figure 26(*a*). The solid line corresponds to the pure Blasius flow, and the dashed line indicates the evolution of the same initial condition when spanwise wall oscillation is introduced. A significantly reduced amplification of perturbation energy is recorded. A qualitatively similar trend is obtained when the optimal initial condition of the Blasius–Stokes flow is used (figure 26*b*). In the subsequent analysis, the focus is on the optimal initial condition for the pure Blasius flow, and the change in the flow response due to the addition of wall oscillation.

At the respective peaks of the energy curves in figure 26, the contribution of the streamwise velocity perturbation, E_u, makes up over 99 % of the total kinetic energy. The origin of the streaks which dominate E_u nevertheless lies in the wall-normal displacement of the mean momentum, and thus in the wall-normal velocity perturbation, v'. The time evolution of the energy in the v' and w' components, E_v and E_w, is presented in figure 27. For pure Blasius flow, E_v decays exponentially. The addition of the spanwise wall oscillation causes a higher decay rate of E_v which is particularly evident in the interval $t \in [0, 20]$. The energy in w' on the other hand increases during this interval in the presence of the wall motion (figure 27*b*).

In order to examine the cause of the rapid decay of v', the perturbation energy equation is considered. For the present base flow $\boldsymbol{U} = (U(y), 0, W(y, t))^{\mathrm{T}}$, the kinetic energy in each of the three components of the velocity perturbation with $\alpha = 0$ is governed by

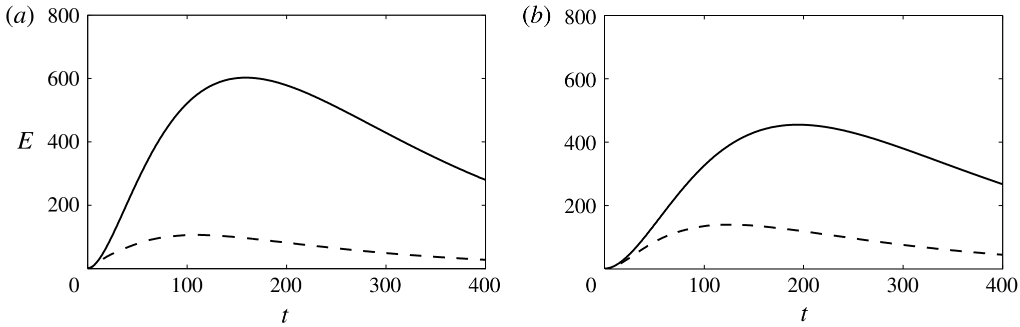

FIGURE 26. Solution of the initial value problem for a base flow described by pure Blasius (solid), and Blasius with wall forcing at $W_0 = 0.25$, $T = 200$ (dashed). (*a*) Optimal initial condition from pure Blasius. (*b*) Optimal initial condition from Blasius with wall forcing.

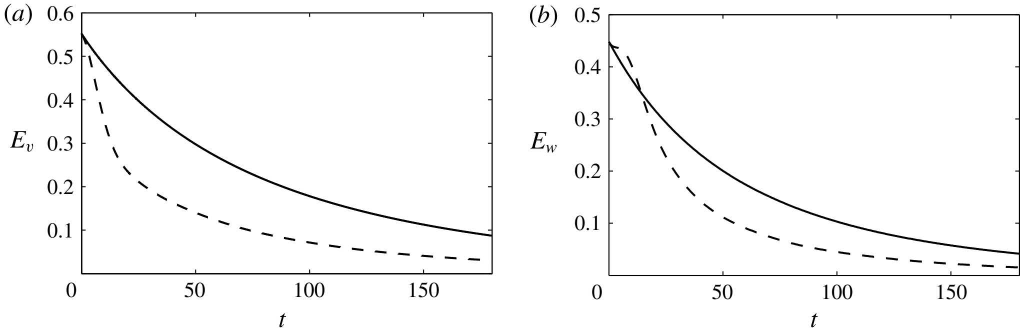

FIGURE 27. Solution of the initial value problem for the optimal perturbation of a Blasius boundary layer for a base flow described by pure Blasius (solid), and Blasius with wall forcing at parameters $W_0 = 0.25$, $T = 200$ (dashed). (*a*) Contribution E_v of the wall-normal perturbation component to the total kinetic energy. (*b*) Contribution E_w of the transverse perturbation component to the total kinetic energy.

$$\frac{\partial E_u}{\partial t} \equiv \int_{\Omega_y} u' \frac{\partial u'}{\partial t}\, \mathrm{d}y = \underbrace{-\int_{\Omega_y} u'v' \frac{\partial U}{\partial y}\, \mathrm{d}y}_{P_u} + \underbrace{\frac{1}{Re} \int_{\Omega_y} u' \frac{\partial^2 u'}{\partial y^2} + u' \frac{\partial^2 u'}{\partial z^2}\, \mathrm{d}y}_{D_u}, \tag{4.16}$$

$$\frac{\partial E_v}{\partial t} \equiv \int_{\Omega_y} v' \frac{\partial v'}{\partial t}\, \mathrm{d}y = \underbrace{-\int_{\Omega_y} v' \frac{\partial p'}{\partial y}\, \mathrm{d}y}_{R_v} + \underbrace{\frac{1}{Re} \int_{\Omega_y} v' \frac{\partial^2 v'}{\partial y^2} + v' \frac{\partial^2 v'}{\partial z^2}\, \mathrm{d}y}_{D_v}, \tag{4.17}$$

$$\begin{aligned} \frac{\partial E_w}{\partial t} &\equiv \int_{\Omega_y} w' \frac{\partial w'}{\partial t}\, \mathrm{d}y \\ &= \underbrace{-\int_{\Omega_y} w'v' \frac{\partial W}{\partial y}\, \mathrm{d}y}_{P_w} \underbrace{- \int_{\Omega_y} w' \frac{\partial p'}{\partial z}\, \mathrm{d}y}_{R_w} + \underbrace{\frac{1}{Re} \int_{\Omega_y} w' \frac{\partial^2 w'}{\partial y^2} + w' \frac{\partial^2 w'}{\partial z^2}\, \mathrm{d}y}_{D_w}. \end{aligned} \tag{4.18}$$

In the presence of the spanwise Stokes layer, the equation for E_w includes a production term analogous to that in the E_u equation. The pressure-redistribution term is,

$$u_j'\frac{\partial p'}{\partial x_j} = -p'\frac{\partial u_j'}{\partial x_j} + \frac{\partial u_j' p'}{\partial x_j}, \tag{4.19}$$

where the repeated index does not imply summation. The first term on the right-hand side of this identity describes redistribution of energy between the velocity components. The second term, referred to as pressure diffusion, is several orders of magnitude smaller than the redistribution term, and is hence ignored.

The energy balance for all three velocity components is presented in figure 28. Starting with the streamwise component, for Blasius flow E_u is driven by a continuous growth of the production term which levels off at $t \approx 60$. The magnitude of the viscous decay term grows as well until it matches the production term at $t = 155$, and the perturbation begins to decay. In the presence of the wall motion, the observed decrease of perturbation energy growth is primarily caused by a significant weakening of the production term, which ceases to increase around $t = 10$. As noted earlier, the cause of the weakening of the streaks is the swift decline of the wall-normal perturbation v' (figure 28*c*,*d*). Without wall oscillation, E_v is weakened due to the combined effect of viscosity and pressure redistribution. The kinetic energy extracted from v' due to the latter term is transferred to the spanwise component, w'. In the presence of the wall forcing, the magnitude of the redistribution term, R_v, increases significantly. The kinetic energy is thus shifted from E_v to E_w, where it is counteracted by a combination of negative production and moderately increased dissipation. The precise balance of E_w is nonetheless immaterial to the streak mechanism: the production term of streamwise perturbations, P_u, is independent of w' and only contains v' – the latter is weakened by the pressure redistribution.

The appreciable increase in the pressure redistribution is explained by considering the Poisson equation which governs the perturbation pressure p',

$$\Delta p' = -2\left(\underbrace{\mathscr{D}U\frac{\partial v'}{\partial x}}_{P1} + \underbrace{\mathscr{D}W\frac{\partial v'}{\partial z}}_{P2}\right). \tag{4.20}$$

While $P1$ vanishes in the limit $\alpha \rightarrow 0$, the finite spanwise wavenumber of the disturbance yields a non-zero $P2$. The spanwise base-flow component W thus supports a pressure perturbation field via $P2$, which is absent in a two-dimensional boundary layer.

In summary, the optimal growth study predicts the weakening of the streaks when spanwise wall motion is added to the Blasius boundary layer. The analysis also explains the origin of this stabilizing influence. The spanwise base flow generates a pressure field that redistributes kinetic energy from the wall-normal perturbations, which play a principal role in streak amplification, into the less critical spanwise perturbation field.

5. Relationship between non-modal and modal growth

So far, two distinct linear mechanisms of primary-perturbation growth have been investigated: the non-modal mechanism that leads to the generation of streaks was demonstrated to be weakened in the presence of the spanwise wall oscillation. At

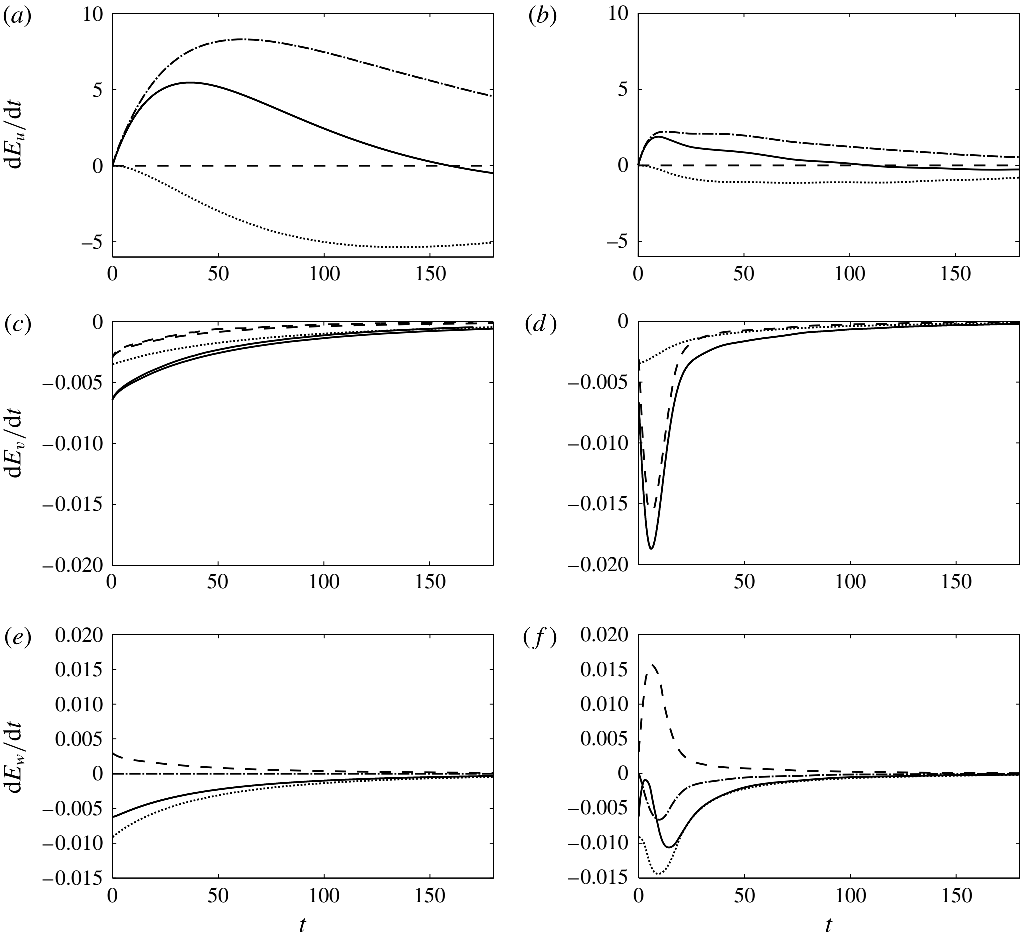

FIGURE 28. Energetic balance for the kinetic energy of the streamwise, wall-normal and spanwise velocity components. Pressure redistribution, R, (dashed), dissipation, D, (dotted), production, P, (dash-dotted), and the sum of the three terms (solid). Left column: (a,c,e) Pure Blasius. Right column: (b,d,f) Forcing with $T = 200$, $W_0 = 0.25$.

the same time, the wall oscillation introduces an inviscid cross-flow-type instability, which for high Re_{Stokes} undermines the stabilizing influence and accelerates breakdown to turbulence. As such, the wall-oscillation amplitude and period dictate whether transition to turbulence is initiated by non-modal or modal primary growth. The relationship between the two mechanisms is explored here.

Previous studies explored the connection between non-modal and exponential instabilities in three-dimensional Falkner–Skan–Cooke boundary layers. Corbett & Bottaro (2001) conducted temporal optimal growth and modal stability analyses. They reported a complementary behaviour of the two mechanisms based on the observed similarity in the shape functions of the perturbations from both approaches. Building on these findings, Tempelmann, Hanifi & Henningson (2010) investigated the spatial optimal growth of three-dimensional boundary layers. Detailed studies around the neutral point of modal instability showed that the optimal disturbances smoothly approach the most unstable eigenmodes as the conditions change from subcritical to

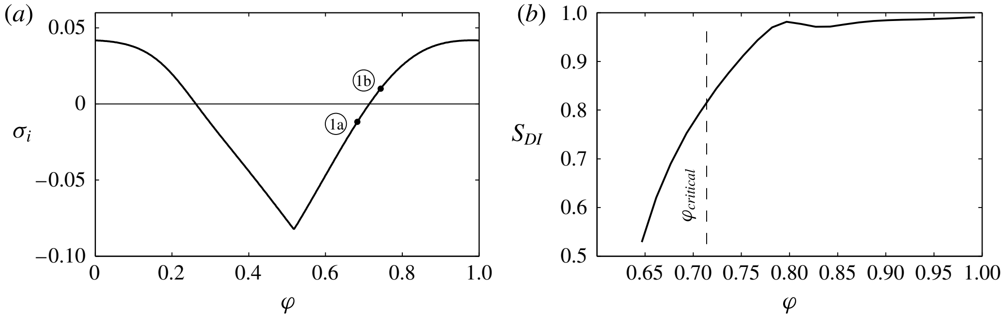

FIGURE 29. (*a*) Temporal growth rate of the instantaneously most unstable discrete mode for $Re = 1800$. (*b*) Energy projection S_{DI} of the solution of optimal growth onto the most unstable discrete mode.

supercritical. Since the present time-dependent base flow can sustain both non-modal and modal growth, it is natural to examine whether the two classes of instabilities coexist and whether one can give rise to the other.

The optimal growth computations presented in § 4 considered the limit of zero streamwise wavenumber, $\alpha = 0$. While this restriction was in line with the objective of explaining the drastic reduction in streak amplitudes in direct numerical simulations, it is no longer meaningful in the context of oblique modal instabilities. The following analysis therefore considers the particular wavenumber pair $(\alpha, \beta) \approx (1.2, 1.4)$, for which the highest growth rates of discrete instabilities were observed (see § 3.2). The modal growth rate σ_i of the most unstable discrete mode as a function of the phase of the base flow is presented in figure 29(*a*). Similar to Tempelmann *et al.* (2010), focus is directed to the variation of the optimal perturbation around the critical point at which discrete modes become unstable.

In order to compare the optimal solution at the final time with the most unstable discrete mode at the same phase, the energy projection

$$S_{DI} = \left\| \int_{\Omega_y} \frac{\boldsymbol{q}_1^H}{\|\boldsymbol{q}_1\|} Q\boldsymbol{e}_m^{DI} \,\mathrm{d}y \right\| \tag{5.1}$$

is considered. In this expression, $\boldsymbol{e}_m^k$ are the instantaneous eigenfunctions normalized to unit energy, $(\boldsymbol{e}_m^k, \boldsymbol{e}_m^k)_E = 1$, and $k = \mathrm{DI}$ identifies the discrete instability mode. An evaluation of S_{DI} is provided in figure 29(*b*) for a range of target phases, $0.65 \leqslant \varphi_1 \leqslant 0.98$ near the critical value, $\varphi_{critical} \approx 0.71$. In all cases, the initial time is $t_0/T = 0.60$. The energy of the optimal disturbance at the target phase is increasingly due to the most unstable discrete mode as the target phase traverses $\varphi_{critical}$. This outcome is qualitatively confirmed in figure 30, which compares the magnitudes of the v' and η' components of the optimal disturbance at target phases $\varphi_{1a} = 0.68$ and $\varphi_{1b} = 0.74$ with the most unstable mode at the respective phases.

The results presented in figures 29 and 30 focused on the make-up of the optimal disturbance at the target phase. The substantial energy contribution by the discrete mode can have two potential implications: first, the disturbance optimal disturbance at the initial phase is a superposition of eigenfunctions which features the most unstable discrete mode more prominently as the target phase approaches $\varphi_{critical}$. A second conjecture is that, during the time evolution of the optimal disturbance from

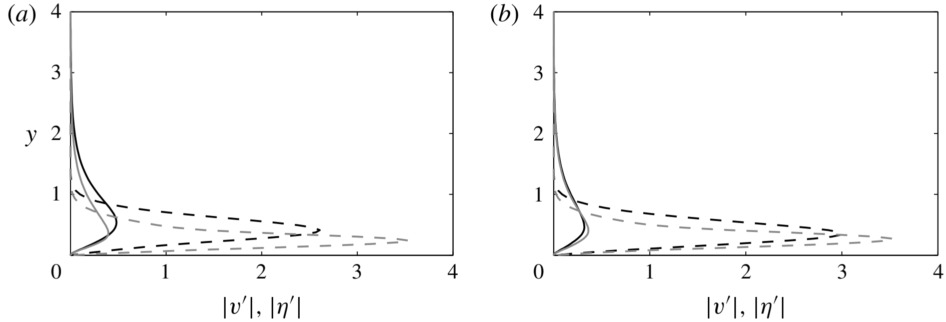

FIGURE 30. Absolute value of the wall-normal velocity (solid) and vorticity (dashed). Optimal disturbance (black) and most unstable discrete mode (grey) at target phase. (*a*) Subcritical target phase, φ_{1a}. (*b*) Supercritical target phase, φ_{1b}.

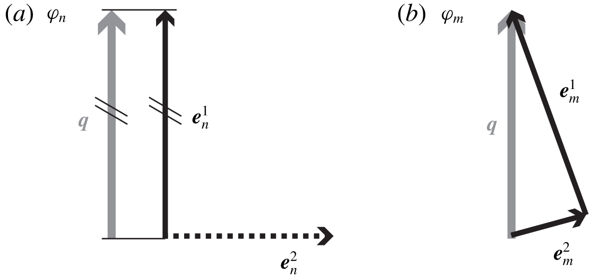

FIGURE 31. Schematic illustrating linear energy transfer between modes in a time-variant base flow. At phase φ_n, the solution vector $\boldsymbol{q}$ is parallel to $\boldsymbol{e}_n^1$. At φ_m the eigenspectrum has changed, and as a consequence the solution $\boldsymbol{q}$ is now a linear combination of $\boldsymbol{e}_m^1$ and $\boldsymbol{e}_m^2$.

its initial condition, the transient growth mechanism transfers energy into the most unstable mode, in particular when the target phase is near or beyond $\varphi_{critical}$. For the current linear system, this energy transfer is only possible via *linear diffraction* by virtue of the time-dependent base flow (Monkewitz & Bunster 1987). A graphical representation of this mechanism is provided in figure 31. At φ_n, the solution $\boldsymbol{q}$ is parallel to eigenvector $\boldsymbol{e}_n^1$, and orthogonal to $\boldsymbol{e}_n^2$. The time dependence of the underlying base state nonetheless alters the spectrum, so that at φ_m, the solution comprises both $\boldsymbol{e}_m^1$ and $\boldsymbol{e}_m^2$. Effectively, this process describes an energy transfer from $\boldsymbol{e}^1$ to $\boldsymbol{e}^2$.

In order to evaluate the energy input into the instability mode due to linear diffraction, each of the eigenfunctions $\boldsymbol{e}_n^j$, which comprise the spectrum at t_0, is normalized to unit energy and separately evolved in time until the final phase $\varphi_1 = 0.98$ is reached. These evolved modes $\boldsymbol{e}_{n,0\Rightarrow 1}^j$ are then expressed in terms of the eigenspectrum at the final time, $\boldsymbol{e}_m^k$,

$$\boldsymbol{e}_{n,0\Rightarrow 1}^j = \sum_k a_k^j \boldsymbol{e}_m^k. \tag{5.2}$$

The coefficients a_k^j are computed by exploiting the bi-orthogonality properties of the forward and adjoint eigenfunctions, $a_k^j = (\boldsymbol{e}_m^{\dagger k}, \boldsymbol{e}_{n,0\Rightarrow 1}^j)_E$, where dagger denotes

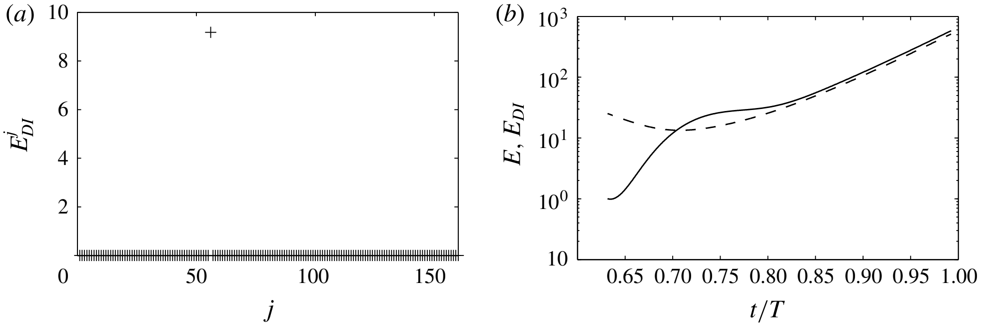

FIGURE 32. (*a*) Norm E_{DI}^j representing intermodal energy transfer into the most unstable discrete mode at $(t/T)_1 = 0.98$. (*b*) Time evolution of the total energy in the optimal disturbance, E, (solid) and of the energy in the discrete mode, E_{DI}, (dashed).

the adjoint. The adjoint eigenfunctions are normalized such that $(\boldsymbol{e}_m^{\dagger l}, \boldsymbol{e}_m^k)_E = \delta_{lk}$ for $(\boldsymbol{e}_m^k, \boldsymbol{e}_m^k)_E = 1$. Let $k = \mathrm{DI}$ designate the index of the discrete instability mode at the final phase. The energy input into DI due to the time evolution of the jth eigenfunction from the initial time is given by

$$E_{DI}^j \equiv (a_{DI}^j)^2. \tag{5.3}$$

An evaluation of E_{DI}^j is provided in figure 32(*a*). It is seen that only one initial mode ($j = 56$) generates an appreciable energy input into the discrete mode at final time. This particular mode is the discrete instability mode at initial time. The extent of intermodal energy transfer by linear diffraction is therefore negligible.

Since the energy is not transferred to the cross-flow instability from other eigenfunctions, it must be present in the initial condition. Figure 32(*b*) demonstrates that this is indeed the case. The solid black line is the time evolution of the energy of the optimal disturbance, $E = (\boldsymbol{q}, \boldsymbol{q})_E$. An initial peak around the critical phase, $\varphi_{critical} = 0.71$, is followed by a second region of growth at supercritical phases. The energy contained in the discrete mode is computed by projecting the state vector $\boldsymbol{q}$ onto the instantaneous set of eigenfunctions $\boldsymbol{e}^k(t/T)$, such that

$$\boldsymbol{q}(t/T) = \sum_k b_k(t/T)\boldsymbol{e}^k(t/T). \tag{5.4}$$

The coefficients $b^k(t/T)$ are again computed using the bi-orthogonality properties of the adjoint. The energy in the discrete instability mode,

$$E_{DI}(t/T) = b_{DI}^2, \tag{5.5}$$

is provided by the dashed line in figure 32. A substantial amount of energy is included in the discrete mode within the optimal initial condition at t_0, but it is masked by the initial cancellation of modes so that the total energy is unity. As time evolves, many of the modes decay, and the total energy approaches that of the discrete mode. The latter is initially decaying, but becomes unstable at the critical phase.

In summary, the observed behaviour ostensibly resembles that reported by Corbett & Bottaro (2001) and Tempelmann *et al.* (2010). The current analysis provides an accurate interpretation: there is no evidence that the exponential instability is initiated by means of intermodal energy transfer. The convergence towards the unstable discrete eigenfunction around the critical point is rather an outcome of the optimization procedure, which preferentially allocates more energy to the instability mode. For this reason, the results presented in this paper have treated the discrete instability separately and optimal growth analysis was only performed for streamwise elongated streaks where the methodology is appropriate.

6. Conclusions

Spanwise wall oscillation can either suppress or promote disturbance growth in pre-transitional boundary layers. DNS results demonstrate that there exists an optimum frequency and amplitude of the spanwise flow for which transition to turbulence is most effectively delayed. Higher wall-oscillation amplitudes can, however, accelerate breakdown compared to an unforced reference case. This behaviour was herein explained in terms of the competition between two amplification mechanisms: the non-modal growth of boundary layer streaks and the exponential amplification of instability modes introduced by the spanwise flow.

Instantaneous instability analyses showed that the superposition of a Blasius boundary layer with a spanwise Stokes layer may lead to exponential perturbation growth, which significantly exceeds that observed for either flow alone. Modal growth strongly depends on the phase of the base state, and intervals of substantial instability are followed by significant decay. As a consequence, the average of the growth rate over a full forcing period is close to zero. Comparison with DNS flow fields demonstrated that, for the current parameter range, instantaneous instability analysis accurately captures the phase-dependent amplification of the disturbances. The instability is inviscid in nature, akin to a cross-flow mode, and its amplification is closely related to the inflection points in the spanwise velocity profile. The generation of new inflection points by the wall motion and their monotonic propagation in the wall-normal dimension leads to mode crossing when tracing the most unstable mode computed in the quasisteady analysis. Continuation of the instability modes showed that at each time instance, the base state encompasses a multiplicity of discrete modes: the presently most unstable eigensolution, as well as the precursors of the most unstable modes of later oscillation cycles coexist.

Optimal growth analyses of boundary layer streaks demonstrated a substantial reduction of the energy gain due to non-modal mechanisms in the presence of the spanwise oscillatory flow. Over a range of downstream Reynolds numbers, the energy amplification is less than half that computed for a pure Blasius boundary layer. In agreement with the direct simulations, the linear analysis predicted an optimum value for the period of the wall forcing for which streak growth is weakest. Unlike the DNS, however, an increase in the amplitude of the wall oscillation is stabilizing in the linear non-modal analysis since the lift-up mechanism is monotonically weakened. The optimal initial condition in the Blasius–Stokes flow consists of a pair of streamwise vortices which are tilted in the spanwise dimension. This configuration enhances the non-modal energy gain by activating the Orr mechanism, which does not contribute to streak formation in two-dimensional boundary layers. The overall weakening of non-modal growth was explained in terms of a rapid decay of wall-normal disturbances, which generate streaks by vertically displacing the mean momentum of the boundary layer. Consideration of the energy balance of the perturbations attributes this decay to a redistribution of kinetic energy from wall-normal to spanwise perturbations due to a pressure field induced by the spanwise base flow.

The relationship between non-modal and modal growth was investigated. Earlier studies had demonstrated that for steady flow over swept wings, the solution of optimal growth calculations smoothly approaches the discrete mode as the Reynolds number is varied around the critical point. This behaviour was reproduced for the Blasius–Stokes base flow. Detailed analyses showed that the discrete mode is already present in the initial condition, although concealed by the simultaneous presence of other modes from the eigenspectrum.

Acknowledgements

The authors are very grateful to Dr Luca Burini for many helpful discussions and for providing the original algorithm for the optimal growth calculations. This work was supported by the Engineering and Physical Sciences Research Council and the National Science Foundation.

Appendix A. Floquet stability

The instantaneous results presented in § 3 explained the phase-dependent perturbation growth observed in the direct numerical simulations. A rigorous approach to the stability analysis of periodic base states, however, requires a global, or Floquet analysis. In the following, results obtained from a Floquet ansatz will be directly compared to the outcome of instantaneous analyses.

For a periodic base flow, $\boldsymbol{U} = (U(y),\, 0,\, W(y,\, t))^{\mathrm{T}}$, where $\boldsymbol{U}(t = kT + a) = \boldsymbol{U}(t = a) \forall\, k \in \mathbb{N}$, a Floquet expansion of the perturbation variables has the form

$$v'(x,\, y,\, z,\, t) = \exp(\sigma^F t) \sum_{n=-\infty}^{\infty} v_n(y) \exp(\mathrm{i}(nF\, t + \alpha x + \beta z)), \tag{A 1}$$

$$\eta'(x,\, y,\, z,\, t) = \exp(\sigma^F t) \sum_{n=-\infty}^{\infty} \eta_n(y) \exp(\mathrm{i}(nF\, t + \alpha x + \beta z)). \tag{A 2}$$

Using this ansatz in the governing equations (3.5) and (3.6) yields

$$\sum_{n=-\infty}^{\infty} \left[(-\mathrm{i}\sigma^F + nF + \alpha U + \beta W)(\mathscr{D}^2 - \kappa^2) - \alpha \mathscr{D}^2 U - \beta \mathscr{D}^2 W + \mathrm{i}\frac{1}{Re}(\mathscr{D}^2 - \kappa^2)^2\right] \\ \times v_n \exp(\mathrm{i}(-\sigma^F + nF)t) = 0, \tag{A 3}$$

$$\sum_{n=-\infty}^{\infty} \left(\left[-\mathrm{i}\sigma^F + nF + \alpha U + \beta W + \mathrm{i}\frac{1}{Re}(\mathscr{D}^2 - k^2)\right] \eta_n - [\alpha \mathscr{D} W - \beta \mathscr{D} U] v_n\right) \\ \times \exp(\mathrm{i}(-\sigma^F + nF)t) = 0, \tag{A 4}$$

which defines an eigenvalue problem in the complex Floquet multiplier, σ^F. The real part of σ^F is a shift from the frequency of the base state. The imaginary part describes the amplification of the associated eigenfunction over a full period of the base state, and may thus be seen as an integral measure for perturbation growth.

Before comparing the results from the instantaneous and Floquet approaches, it is helpful to recall characteristic properties of both methodologies. One evident difference between the two approaches is periodicity of the individual eigensolutions, which is enforced in the Floquet framework. The earlier instantaneous results, on the other hand, captured a mode crossing and an associated sudden change in the eigenfunction as the phase of the base flow was changed. The mode crossing was attributed to the generation of new inflection points and their propagation in the wall-normal direction. Furthermore, only the Floquet approach incorporates linear energy diffraction (Monkewitz & Bunster 1987): in an unsteady base state, the time evolution of a perturbation describes a continuous reprojection of the solution onto the current eigenbasis (see § 5). Since the change in the continuation of an eigenfunction of the instantaneous base flow between t and $t + \Delta t$ is generally not identical to its time evolution from t to $t + \Delta t$, the difference in energy must be absorbed by the remaining modes. This effectively describes a linear mechanism for intermodal energy transfer and explains why, even in cases where the instantaneous solution is periodic, the time-averaged instantaneous growth rate may differ from the Floquet multiplier. It should be noted, however, that Luo & Wu (2010) found this deviation to be negligible for pure Stokes layers in the present parameter range.

The quantity gained from an instantaneous instability analysis that is most suitable for comparison with the Floquet multiplier is the averaged temporal growth rate $\sigma_{i,avg}$. For the particular wavenumber pair $(\alpha, \beta) = (1.2, 1.4)$ which yields the highest instantaneous growth rate, $\sigma_{i,avg} = -0.0012$ was obtained using the analysis in § 3.2. The Floquet analysis predicts a growth rate, $\sigma^F = -0.0364$. Both approaches therefore predict global stability, with the Floquet mode decaying at a higher rate. The difference in the decay rate is examined further.

While σ^F itself only describes 'global' growth over full periods, the Floquet analysis also provides an eigenfunction, which is valid for all $t \in [0, T]$. A norm which describes the kinetic energy in the state vector $\boldsymbol{q}$ is given by

$$E \equiv \left\| \int_{\Omega_y} \boldsymbol{q}^H \boldsymbol{Q} \boldsymbol{q} \, \mathrm{d}y \right\|, \tag{A 5}$$

where

$$\boldsymbol{Q} = \begin{bmatrix} k^2 - \mathscr{D}^2 & 0 \\ 0 & 1 \end{bmatrix}. \tag{A 6}$$

In terms of this norm, the temporal growth rate of the instantaneous analysis is recovered from the relation

$$\sigma_i(t) = \frac{1}{2\,\delta t} \ln \frac{E(t+\delta t)}{E(t)}. \tag{A 7}$$

Evaluation of this expression for the Floquet mode provides a momentary energy-amplification rate σ_i^m, which may be compared to the modal growth rates obtained from instantaneous analyses. Both quantities are presented in figure 33(*a*). The maximum value of the instantaneous growth rates, $\sigma_i = 0.043$, matches that of the Floquet result, σ_i^m. Between $t/T = 0.2$ and $t/T = 0.85$, the Floquet growth rate smoothly decays and remains unaffected by the mode crossing associated with the newly formed inflection point. Instead, the Floquet mode gradually departs from the instantaneous growth rate in order to form a periodic solution.

A quantitative measure for the congruence between the instantaneous and Floquet modes is given by the projection

$$S_{FX} \equiv \left\| \int_{\Omega_y} \boldsymbol{e}_F^H \boldsymbol{Q} \boldsymbol{e}_X \, \mathrm{d}y \right\|. \tag{A 8}$$

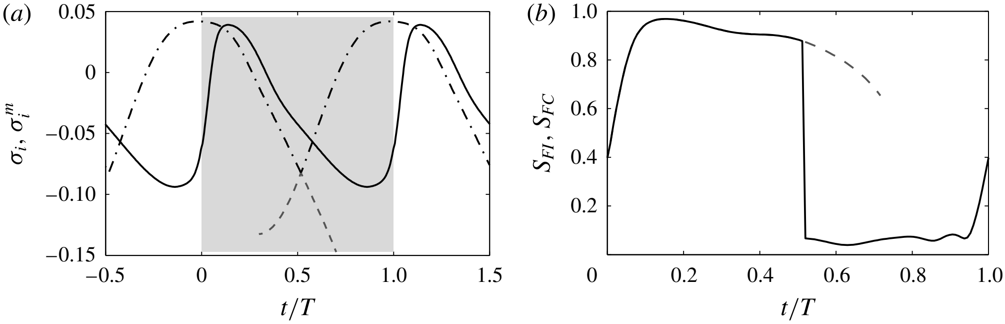

FIGURE 33. (*a*) Momentary energy-amplification rate σ_i^m of the Floquet mode (solid), temporal growth rate σ_i of the instantaneously most unstable discrete mode (dash-dotted), and continuation of the most unstable instantaneous mode at $t/T = 0$ (dashed). (*b*) Energy projections S_{FI} of Floquet mode and instantaneously most unstable mode (solid), and S_{FC} of Floquet mode and continuation of the most unstable instantaneous mode at $t/T = 0$ (dashed).

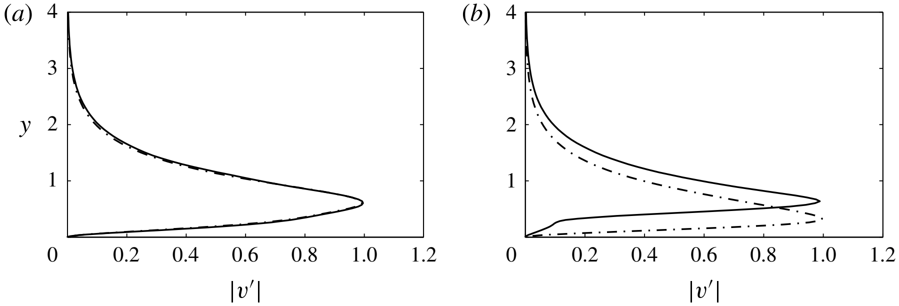

FIGURE 34. Eigenfunctions at selected phases. Floquet mode (solid) and instantaneously most unstable mode (dash-dotted). Absolute value of the wall-normal velocity component, $|v'|$, normalized to unit magnitude: (*a*) $t/T = 0.13$; (*b*) $t/T = 0.63$.

Here, $\boldsymbol{e}_F$ is the Floquet eigenfunction normalized to unit energy and $\boldsymbol{e}_X$ is either the instantaneously most unstable mode (index I) or the continuation of the mode which is most unstable at $t/T = 0$ (index C). Figure 33(*b*) shows that, at the mode crossing, the projected kinetic energy S_{FI} between the instantaneously most unstable mode and the Floquet mode sharply decreases.

The absolute values of the eigenfunctions of the two modes, normalized to unit magnitude, are presented in figure 34 for two phases of the base state. Ahead of the mode crossing, at $t/T = 0.13$, the dependence of the two modes on y is virtually identical. At the second considered phase, $t/T = 0.63$, the instantaneous mode has moved towards the wall while the maximum of the shape function of the Floquet mode remains at the same position.

In summary, the recurring generation and propagation of the inflection points in the wall-normal direction leads to a crossing of the instantaneously most unstable modes. A mode is associated with an inflection point and, as it traces its path towards the edge of the boundary layer, its growth rate decreases. Another mode emerges as the most unstable with the generation of a new inflection point. In the Floquet analysis, on the other hand, the most unstable global eigenmode is fundamental and does not capture this behaviour. Instead, the Floquet analysis predicts a periodic mode that persists over many cycles. In a realistic flow with background noise, instabilities can repeatedly emerge due to the new inflection points. As such, the analysis of the instantaneous flow provides a good measure of momentary amplification rates, whereas the Floquet analysis provides a measure of the average growth rate including periods of decay.

Appendix B. Optimal disturbances

B.1. *Governing equations*

Let $\boldsymbol{q} = (v,\ \eta)^{\mathrm{T}}$, then the time evolution of small perturbations of the wall-normal velocity v and the wall-normal vorticity η is described by the initial value problem

$$\underbrace{\left(\boldsymbol{L} - \boldsymbol{M}\frac{\partial}{\partial t}\right)}_{\boldsymbol{B}} \boldsymbol{q} = 0 \tag{B 1}$$

with

$$\boldsymbol{M} = \begin{bmatrix} \mathscr{D}^2 - k^2 & 0 \\ 0 & 1 \end{bmatrix} \quad \text{and} \quad \boldsymbol{L} = \begin{bmatrix} L_{OS} & 0 \\ C & L_{SQ} \end{bmatrix}, \tag{B 2a,b}$$

where

$$L_{OS} = (-\mathrm{i}\alpha U - \mathrm{i}\beta W)(\mathscr{D}^2 - k^2) + \mathrm{i}\alpha\mathscr{D}^2 U + \mathrm{i}\beta\mathscr{D}^2 W + \frac{1}{Re}(\mathscr{D}^2 - k^2)^2, \tag{B 3}$$

$$L_{SQ} = -\mathrm{i}\alpha U - \mathrm{i}\beta W + \frac{1}{Re}(\mathscr{D}^2 - k^2) \quad \text{and} \quad C = \mathrm{i}(\alpha\mathscr{D}W - \beta\mathscr{D}U). \tag{B 4a,b}$$

The associated boundary conditions for the spatial domain $\varOmega_y$ are

$$v = 0, \quad \mathscr{D}v = 0, \quad \eta = 0 \quad \text{on } \partial\varOmega_y. \tag{B 5a–c}$$

B.2. *Adjoint problem*

Under the norm $\langle \boldsymbol{q}_A, \boldsymbol{q}_B \rangle \equiv \int_{\varOmega_t}\int_{\varOmega_y} \boldsymbol{q}_A^H \boldsymbol{q}_B \,\mathrm{d}y\,\mathrm{d}t$, the adjoint of the operator $\boldsymbol{B}$ is defined as,

$$\langle \boldsymbol{q}^{\dagger}, \boldsymbol{B}\boldsymbol{q} \rangle = \langle \boldsymbol{B}^{\dagger}\boldsymbol{q}^{\dagger}, \boldsymbol{q} \rangle + \text{boundary terms}. \tag{B 6}$$

Integration by parts of the left-hand side of (B 6) gives

$$\left\langle \boldsymbol{q}^{\dagger}, \underbrace{\left(\boldsymbol{L} - \boldsymbol{M}\frac{\partial}{\partial t}\right)}_{\boldsymbol{B}} \boldsymbol{q} \right\rangle = \left\langle \underbrace{\left(\boldsymbol{L}^{\dagger} + \boldsymbol{M}^{\dagger}\frac{\partial}{\partial t}\right)}_{\boldsymbol{B}^{\dagger}} \boldsymbol{q}^{\dagger}, \boldsymbol{q} \right\rangle - \int_{\varOmega_y} [\boldsymbol{q}^{\dagger H}\boldsymbol{M}\boldsymbol{q}]_{t_0}^{t_1}\,\mathrm{d}y + \text{boundary terms in } y. \tag{B 7}$$

Comparison of the coefficients yields

$$\boldsymbol{M}^{\dagger} = -\begin{bmatrix} \mathscr{D}^2 - k^2 & 0 \\ 0 & 1 \end{bmatrix} \quad \text{and} \quad \boldsymbol{L}^{\dagger} = \begin{bmatrix} L_{OS}^{\dagger} & C^{\dagger} \\ 0 & L_{SQ}^{\dagger} \end{bmatrix}. \tag{B 8a,b}$$

The second term on the right-hand side is zero under the matching conditions (4.10) and (4.11). Furthermore, choice of

$$v^\dagger = 0, \quad \mathscr{D}v^\dagger = 0, \quad \eta^\dagger = 0 \quad \text{on } \partial\varOmega_y \tag{B 9a–c}$$

together with (B 5) causes the boundary terms in y to vanish.

REFERENCES

Akhavan, R., Kamm, R. D. & Shapiro, A. H. 1991 An investigation of transition to turbulence in bounded oscillatory Stokes flows. Part 1. Experiments. *J. Fluid Mech.* **225**, 395–422.

Andersson, P., Berggren, M. & Henningson, D. S. 1999 Optimal disturbances and bypass transition in boundary layers. *Phys. Fluids* **11** (1), 134–150.

Andersson, P., Brandt, L., Bottaro, A. & Henningson, D. S. 2001 On the breakdown of boundary layer streaks. *J. Fluid Mech.* **428**, 29–60.

Bippes, H. 1999 Basic experiments on transition in three-dimensional boundary layers dominated by crossflow instability. *Prog. Aerosp. Sci.* **35**, 363–412.

Blennerhassett, P. J. & Bassom, A. P. 2002 The linear stability of flat Stokes layers. *J. Fluid Mech.* **464**, 393–410.

Blesbois, O., Chernyshenko, S. I., Touber, E. & Leschziner, M. A. 2013 Pattern prediction by linear analysis of turbulent flow with drag reduction by wall oscillation. *J. Fluid Mech.* **724**, 607–641.

Brandt, L. 2014 The lift-up effect: The linear mechanism behind transition and turbulence in shear flows. *Eur. J. Mech.* (*B/Fluids*) **47**, 80–96.

Brandt, L., Schlatter, P. & Henningson, D. S. 2004 Transition in boundary layers subject to free-stream turbulence. *J. Fluid Mech.* **517**, 167–198.

Butler, K. M. & Farrell, B. F. 1992 Three-dimensional optimal perturbations in viscous shear flow. *Phys. Fluids* A **4** (8), 1637–1650.

Clarion, C. & Pelissier, R. 1975 A theoretical and experimental study of the velocity distribution and transition to turbulence in free oscillatory flow. *J. Fluid Mech.* **70**, 59–79.

Corbett, P. & Bottaro, A. 2001 Optimal linear growth in swept boundary layers. *J. Fluid Mech.* **435**, 1–23.

Cowley, S. J. 1987 High frequency Rayleigh instability of Stokes layers. In *Stability of Time Dependent and Spatially Varying Flows* (ed. D. L. Dwoyer & M. Y. Hussaini), pp. 244–260. Springer.

Davis, S. H. 1976 The stability of time-periodic flows. *Annu. Rev. Fluid Mech.* **8**, 57–74.

Deyhle, H. & Bippes, H. 1996 Disturbance growth in an unstable three-dimensional boundary layer and its dependence on environmental conditions. *J. Fluid Mech.* **316**, 73–113.

Deyhle, H., Hoehler, G. & Bippes, H. 1993 Experimental investigation of instability wave propagation in a three-dimensional boundary-layer flow. *AIAA J.* **31** (4), 637–645.

Duque-Daza, C. A., Baig, M. F., Lockerby, D. A., Chernyshenko, S. I. & Davies, C. 2012 Modelling turbulent skin-friction control using linearized Navier–Stokes equations. *J. Fluid Mech.* **702**, 403–414.

Golub, G. H. & Van Loan, C. F. 1996 *Matrix Computations*, 3rd edn. The Johns Hopkins University Press.

Hack, M. J. P. & Zaki, T. A. 2012 The continuous spectrum of time-harmonic shear layers. *Phys. Fluids* **24** (3), 034101.

Hack, M. J. P. & Zaki, T. A. 2014*a* The influence of harmonic wall motion on transitional boundary layers. *J. Fluid Mech.* **760**, 63–94.

Hack, M. J. P. & Zaki, T. A. 2014*b* Streak instabilities in boundary layers beneath free-stream turbulence. *J. Fluid Mech.* **741**, 280–315.

Hall, P. 1978 The linear stability of flat Stokes layers. *Proc. R. Soc. Lond.* A **359**, 151–166.

Hall, P. 2003 On the instability of Stokes layers at high Reynolds numbers. *J. Fluid Mech.* **482**, 1–15.

HINO, M., SAWAMOTO, M. & TAKASU, S. 1976 Experiments on transition to turbulence in an oscillating pipe flow. *J. Fluid Mech.* **75**, 193–207.

HUNT, J. C. R. & CARRUTHERS, D. J. 1990 Rapid distortion theory and the 'problems' of turbulence. *J. Fluid Mech.* **212**, 497–532.

JACOBS, R. G. & DURBIN, P. A. 1998 Shear sheltering and the continuous spectrum of the Orr–Sommerfeld equation. *Phys. Fluids* **10** (8), 2006–2011.

JACOBS, R. G. & DURBIN, P. A. 2001 Simulations of bypass transition. *J. Fluid Mech.* **428**, 185–212.

KOCH, W., BERTOLOTTI, F. P., STOLTE, A. & HEIN, S. 2000 Nonlinear equilibrium solutions in a three-dimensional boundary layer and their secondary instability. *J. Fluid Mech.* **406**, 131–174.

LANDAHL, M. T. 1975 Wave breakdown and turbulence. *SIAM J. Appl. Maths* **28** (4), 735–756.

LANDAHL, M. T. 1980 A note on an algebraic instability of inviscid parallel shear flows. *J. Fluid Mech.* **98**, 243–251.

LUO, J. & WU, X. 2010 On the linear instability of a finite Stokes layer: instantaneous versus Floquet modes. *Phys. Fluids* **22**, 054106.

MANDAL, A. C., VENKATAKRISHNAN, L. & DEY, J. 2010 A study on boundary-layer transition induced by free-stream turbulence. *J. Fluid Mech.* **660**, 114–146.

MATSUBARA, M. & ALFREDSSON, P. 2001 Disturbance growth in boundary layers subjected to free-stream turbulence. *J. Fluid Mech.* **430**, 149–168.

MERKLI, P. & THOMANN, H. 1975 Transition to turbulence in oscillating pipe flow. *J. Fluid Mech.* **68**, 567–575.

MONKEWITZ, P. A. & BUNSTER, A. 1987 The stability of the Stokes layer: visual observations and some theoretical considerations. In *Stability of Time Dependent and Spatially Varying Flows* (ed. D. L. Dwoyer & M. Y. Hussaini), pp. 244–260. Springer.

MORKOVIN, M. V. & OBREMSKI, H. J. 1969 Application of a quasi-steady stability model to periodic boundary-layer flows. *AIAA J.* **7** (7), 1298–1301.

NAGARAJAN, S., LELE, S. K. & FERZIGER, J. H. 2007 Leading-edge effects in bypass transition. *J. Fluid Mech.* **572**, 471–504.

NOLAN, K. P. & ZAKI, T. A. 2013 Conditional sampling of transitional boundary layers in pressure gradients. *J. Fluid Mech.* **728**, 306–339.

RADEZTSKY, R. H., REIBERT, M. S. & SARIC, W. S. 1999 Effect of isolated micron-sized roughness on transition in swept-wing flows. *AIAA J.* **37** (11), 1370–1377.

RICCO, P. 2011 Laminar streaks with spanwise wall forcing. *Phys. Fluids* **23**, 064103.

SARIC, W. S., REED, H. L. & WHITE, E. B. 2003 Stability and transition of three-dimensional boundary layers. *Annu. Rev. Fluid Mech.* **35**, 413–440.

SCHMID, P. J. 2007 Nonmodal stability theory. *Annu. Rev. Fluid Mech.* **39**, 129–162.

SCHRADER, L.-U., BRANDT, L. & HENNINGSON, D. S. 2009 Receptivity mechanisms in three-dimensional boundary-layer flows. *J. Fluid Mech.* **618**, 209–241.

SCHRADER, L.-U., SUBIR, A. & BRANDT, L. 2010 Transition to turbulence in the boundary layer over a smooth and rough swept plate exposed to free-stream turbulence. *J. Fluid Mech.* **646**, 297–325.

TEMPELMANN, D., HANIFI, A. & HENNINGSON, D. S. 2010 Spatial optimal growth in three-dimensional boundary layers. *J. Fluid Mech.* **646**, 5–37.

THOMAS, C., BASSOM, A. P., BLENNERHASSETT, P. J. & DAVIES, C. 2011 The linear stability of oscillatory poiseuille flow in channels and pipes. *Proc. R. Soc. Lond.* A **467**, 2643–2662.

VAUGHAN, N. J. & ZAKI, T. A. 2011 Stability of zero-pressure-gradient boundary layer distorted by unsteady Klebanoff streaks. *J. Fluid Mech.* **681**, 116–153.

VON KERCZEK, C. & DAVIS, S. H. 1974 Linear stability theory of oscillatory Stokes layers. *J. Fluid Mech.* **62**, 753–773.

WASSERMANN, P. & KLOKER, M. 2002 Mechanisms and passive control of crossflow-vortex-induced transition in a three-dimensional boundary layer. *J. Fluid Mech.* **456**, 49–84.

WHITE, E. B. & SARIC, W. S. 2005 Secondary instability of crossflow vortices. *J. Fluid Mech.* **525**, 275–308.

ZAKI, T. A. & SAHA, S. 2009 On shear sheltering and the structure of vortical modes in single- and two-fluid boundary layers. *J. Fluid Mech.* **626**, 111–147.